electronics

Article

Development of Single-Phase Synchronous Inverter for Single-Phase Microgrid

Naoto Yorino [1,2], Yoshifumi Zoka [2], Yutaka Sasaki [2,*], Shinya Sekizaki [2], Mitsuo Yokonuma [3,*], Takahiro Himuro [3], Futoshi Kuroki [3], Toshinori Fujii [3] and Hirotaka Inoue [3]

1 National Institute of Technology (KOSEN), Kure College, Kure 737-8506, Japan; yorino@hiroshima-u.ac.jp
2 Graduate School of Advanced Science and Engineering, Hiroshima University, Higashihiroshima 739-8527, Japan; zo@hiroshima-u.ac.jp (Y.Z.); sekizaki@hiroshima-u.ac.jp (S.S.)
3 Department of Electrical Engineering and Information Science, National Institute of Technology (KOSEN), Kure College, Kure 737-8506, Japan; t-himuro@kure-nct.ac.jp (T.H.); kuroki@kure.kosen-ac.jp (F.K.); t_fujii@kure-nct.ac.jp (T.F.); hiro@kure-nct.ac.jp (H.I.)
* Correspondence: yusasaki@hiroshima-u.ac.jp (Y.S.); yokonuma@kure-nct.ac.jp (M.Y.)

Abstract: The work is based on a collaboration between Hiroshima University and Kure KOSEN College. This paper presents the design concept, hardware, and applications of a single-phase synchronous inverter (SSI), a specially designed grid-forming inverter (GFM) for single-phase microgrid (SMGs). The SSI is designed for the conventional 100/200 V distribution network and is based on the concept of "Non-Interference Core (NIC) dynamic model". Novel contributions of this paper are: (1) A root mean square (RMS) model of NIC-SSI was developed, combined with the conventional power system model, and verified through the comparison with the hardware-in-the-loop (HIL) simulation and SSI hardware experiments; (2) using the developed RMS simulation tool, the stabilization effect of the SSIs was investigated in condition under which the SSIs are massively installed in a distribution system; (3) off-grid SMG operations using SSIs under various ill-conditioned loads were demonstrated. The results show that the SSI has the considerable ability of grid stability enhancements for frequency, transient, and small-signal stabilities. The proposed SMG using SSIs is promising.

Keywords: power systems; frequency stability; transient stability; single-phase synchronous inverter; RMS simulation

Citation: Yorino, N.; Zoka, Y.; Sasaki, Y.; Sekizaki, S.; Yokonuma, M.; Himuro, T.; Kuroki, F.; Fujii, T.; Inoue, H. Development of Single-Phase Synchronous Inverter for Single-Phase Microgrid. *Electronics* **2024**, *13*, 478. https://doi.org/10.3390/electronics13030478

Academic Editor: Adel M. Sharaf

Received: 28 November 2023
Revised: 9 January 2024
Accepted: 9 January 2024
Published: 23 January 2024

1. Introduction

Recently, power system stability has faced many challenges with the large-scale integration of variable renewable energy (VRE) sources. The major challenge is replacing conventional synchronous machines with inverter-based resources (IBRs) whose behavior and interaction with the power system are not fully understood. As a result, frequency stability [1–4] problems emerge, such as the degradation in the rate of change of frequency (RoCoF) and frequency nadir due to the decreasing rotational inertia of power systems. Thus, developing countermeasures against these problems has become an urgent issue [5–7].

New operation standards are under examination in the United Kingdom, Ireland, Australia, and the United States, where VRE installations have increased extremely [8–10]. For example, a new frequency service, such as fast frequency response (FFR), has been designed. Grid operators around the world specify their individual operating rules for frequency change in response to several disturbances in the power system.

Grid-forming inverters (GFMs) are expected to solve these problems. However, it is difficult to verify the stabilization effect since no suitable inverter models fully satisfy the requirements of power system stability analysis [11,12]. The inverters used in VRE sources and storage batteries are required to contribute to power system stability, especially frequency stability. Thus, the GFM, which controls its frequency and voltage output, plays a constructive role in improving the frequency dynamics and stability of the power system. There are various types of controls for GFMs, such as virtual synchronous machine (VSM) [13–15] synchronverters [16,17], the swing equation of the synchronous machine, power synchronization [18,19], and droop control [20]. In addition, authors have developed several methods and proposals for network stabilization using the synchronous inverter. The works include a pseudo-synchronization power controller for single and three-phase voltage source converters (VSCs) and other studies for assessing the effectiveness of pseudo-synchronizing power, voltage control, frequency control, power system stabilization [21]. A single-phase synchronous inverter (SSI) was developed using a novel design method for GFM, based on a non-interference core (NIC) concept in [22]. The NIC-SSI was constructed to act dynamically the same as a conventional synchronous machine, to solve recent IBR problems, and to stabilize the power system.

There exist various GFM approaches and projects for the enhancement of power system stability such as [23–33], which are all effective methods applied to general three-phase systems. In Europe, many demonstration tests have been conducted using wind power with grid-forming functionality implemented, connecting to the power grid [23,26–29]. In the United States, verification and evaluation are being performed, focusing on the interoperability of the grid and inverters [30,31]. In Australia, grid stabilization using large-scale storage batteries with grid-forming functionality implemented is being demonstrated [32,33]. Above all, these projects use large-scale three-phase GFM inverters.

On the other hand, no major realistic ideas are being discussed about the countermeasures for low-voltage single-phase distribution systems for the enhancement of bulk power system stability by introducing new GFM devices. This is also the case in Japan, but various realistic approaches have been studied in the NEDO (New Energy and Industrial Technology Development Organization, national research and development agency) project, where we have confirmed the effectiveness of the proposed single-phase approach.

This paper presents our recent work on single-phase GFM applications. The novel contributions of this paper are:

- An RMS model of NIC-SSI in [34] is combined with the conventional power system model to develop an RMS simulation tool;
- The developed root mean square (RMS) simulation tool is verified through the comparison with hardware-in-the-loop (HIL) simulation, and SSI hardware experiments;
- Using the developed simulation and analysis tools, the stabilization effect of the SSIs is investigated in a condition where SSIs are massively installed in a distribution system;
- The stability of off-grid SMG operation is confirmed under various conditions including ill-conditioned loads.

The installation of GFM on the single-phase consumer side is assumed as a new concept, and specially designed hardware is introduced for grid stabilization. The simulation results in a three-machine nine-bus system show that the SSI has the considerable ability of grid stabilization concerning frequency, transient, and small-signal stabilities. Thus, the resilience of power systems in a normal state is improved.

The final part of the paper investigates SMG operations in emergencies stemming from possible natural disasters. The conceptional planning and experimental performance of the SMG are presented based on [34] together with recent additional experimental studies on off-grid SMG operations. The results of hardware experiments show that the SSI can realize robust off-grid operations even with ill-conditioned loads. All of the results in this paper imply that the SMG using SSI is promising.

The remainder of the paper is divided into five sections, organized as follows. Section 2 summarizes our previous works explaining the NIC design method, which provides the theoretical background for the stabilization of grids including SMGs by the proposed SSI. The SSI model and its hardware are also introduced in this section. Section 3 proposes an RMS simulation tool based on the NIC design method, in which the NIC design method explained in Section 2 is directly applied to the SSI model and the conventional power system model to obtain the RMS simulation model. The developed RMS simulation tool is verified through laboratory experiments using the developed hardware and HIL simulations. In Section 4, the effect of SSI on power system stability is evaluated using the developed RMS simulation tool, where a standard power system, the Anderson–Fouad nine-bus three-generator system, is analyzed from the viewpoint of the most critical stability issues, which are frequency stability, transient stability, and small-signal stability. Section 5 performs experimental studies on the stability and feasibility issues of the SMG, where the grid is operated only by SSIs with no conventional generators. Conclusions and future studies are explored in Section 6.

2. Design Concept of the SSI

2.1. Problem Description

This section describes problems associated with introducing IBRs into the power system:

1. Recent power systems, including MGs, are facing stability problems due to the increase in IBRs [35]. Therefore, a new type of GFM inverter is being studied for power system stabilization;
2. RMS analysis has been used widely in the assessment of power system stability, which is becoming more difficult with increasing IBRs. Therefore, a reliable method is required for stability evaluation as well as an effective control design method for IBRs.

2.2. NIC Control Design for the SSI

The NIC design concept for he GFM inverter was proposed in [21,22,34,36], has been upgraded to date to solve the problems stated in the previous subsection. The proposed method can be described as below:

The time-scale separation method, shown in Figure 1, is used to develop the NIC design based on the singular perturbation theory. The method has been widely used, such as in voltage stability analysis [37]. Based on the time-scale separation, when the original power system, including IBRs, is divided into slow and fast dynamics as shown in Figure 1, it can be approximated by the slow and fast subsystems, (f2) and (f3). The slow variables, x_s, are governed by the dynamic equation of the slow subsystem (f2), while the fast dynamics, x_F, are determined by the fast subsystem (f3). Therefore, the original system is stable when both subsystems are stable. Based on this theory, the complex phenomenon of the power system with IBRs can be analyzed theoretically in the following proposed approach.

1. The slow dynamic of the inverter that corresponds to the slow subsystem is called the core. The controller for stabilizing the power system is modeled here. The other inverter dynamic, the overall fast dynamic is called the shell, which belongs the fast subsystem. This treatment makes the independent design of the slow and fast dynamics possible. The original power system is stable if, and only if, both the subsystems are stable.
2. The fast subsystem must be stable for power system operation. For this purpose, the shell must be stable under any operating conditions. Therefore, in this paper, destabilizing factors, including all inner loops and those with high-frequency characteristics, are eliminated as much as possible. (Instead of the inner loop of current control, effective overcurrent suppression is proposed in [38].)
3. The slow subsystem can approximate the original system with high accuracy when the fast subsystem is stable. In this case, the slow subsystem consisting of shells with the conventional RMS model of a power system can be used as an RMS simulation model, as given in Figure 1, which will be proposed in Section 3.1. This also implies that power system stabilization can be achieved by proper design of the inverter shell.
4. Although all the NIC design functions have not been reached up to now, this paper presents the effectiveness of the abovementioned NIC-based design of inverters. Actual experiments were conducted with this design to show that the inverter can be operated in a practical manner, stabilizing the power system.

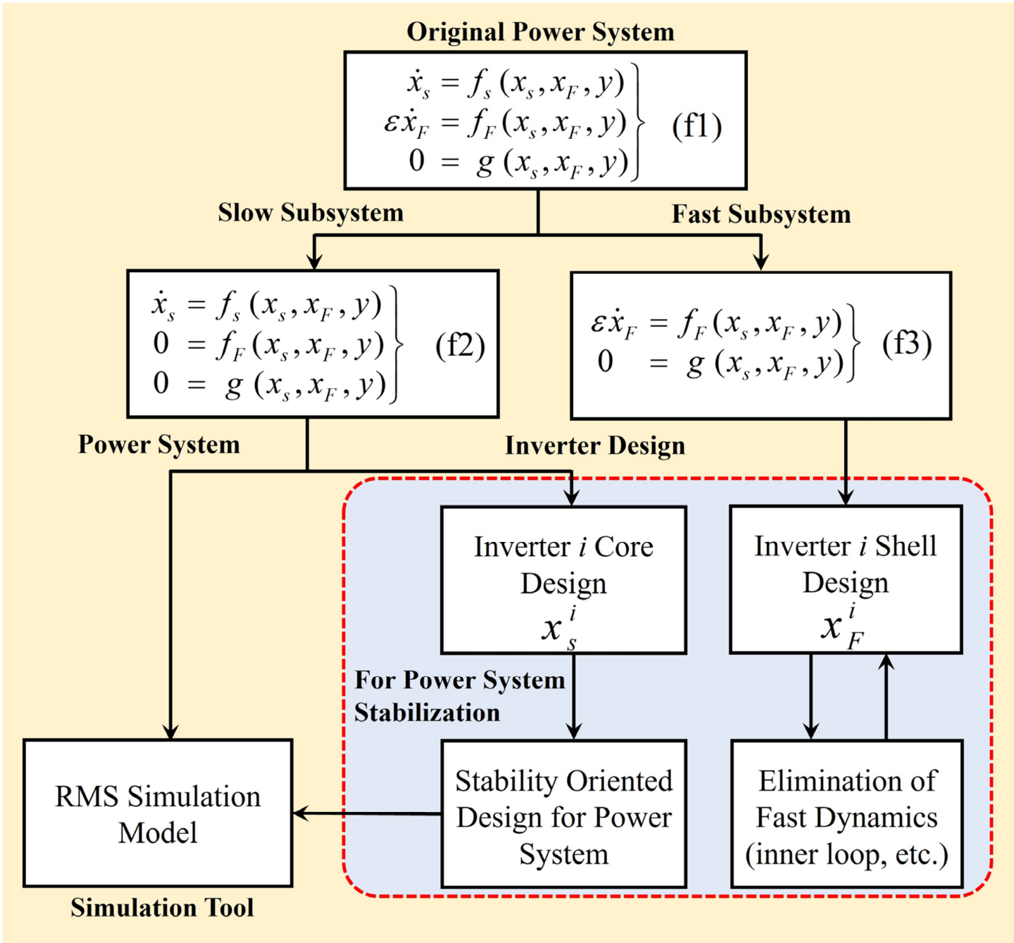

Figure 1. NIC design based on the time-scale separation. The dotted line part represents i-th inverter dynamics.

The developed SSI is a GFM-type inverter with a highly stabilizing effect that connects to the main grid in normal operation, and it can form an MG even in emergencies. Moreover, the authors proposed the NIC design method, implying that the SSI works ideally like an analog computer, governed strictly by the implemented core dynamics.

2.3. SSI Model Configuration

The proposed SSI is based on a full-bridge inverter circuit to convert the DC link voltage V_{DC} to AC voltage v^{inv}, as shown in Figure 2. A storage battery is connected to the DC side to transfer the active power. On the AC side, an inductance L is connected for output smoothing (X in Figure 2), and the SSI is connected to the external grid through the inductance L. The active power output P_e to the grid is exchanged based on the mutual relationship between the SSI terminals and the internal electromotive force (EMF).

Figure 3 shows the block diagram of the developed SSI controller. Where v^{inv} is the SSI output voltage (RMS: V^{inv}), v^{grid} is the grid voltage (RMS: V^{grid}), ω_{inv} is the internal frequency of the SSI, θ_{inv} is the pseudo-rotor angle of the SSI, i^{inv} is the SSI output current (RMS: I^{inv}), V_{ref} is the reference voltage, Q_{ref} is the reactive power reference, α is the α-axis components, β is the β-axis components, P_m is the virtual mechanical input of the SSI, P_e is the active power output, and Q_e is the reactive power output.

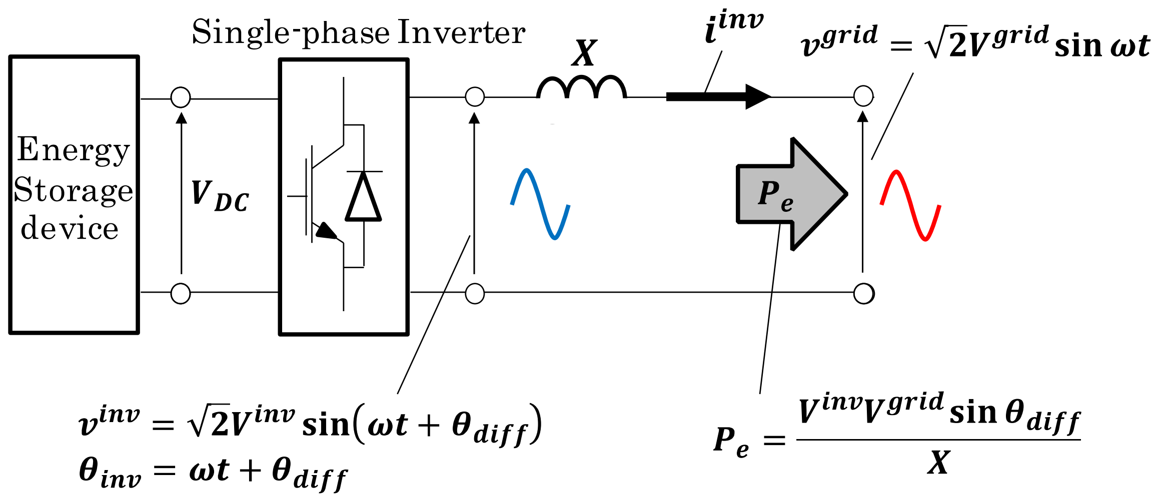

Figure 2. The single-phase synchronous inverter model.

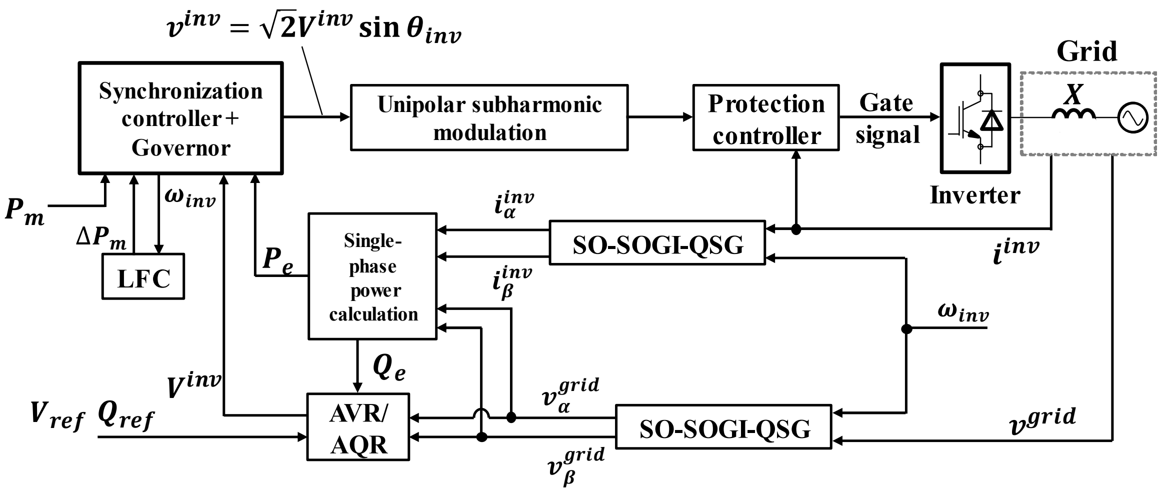

Figure 3. The proposed SSI controller.

In the proposed model, θ_{inv}, which is equivalent to the dynamic characteristics caused by the rotating magnetic field, is calculated based on the swing equation, and the inverter output voltage is controlled based on θ_{inv} to ensure stable synchronization with the single-phase system. In a single-phase circuit with a supply frequency ω, the instantaneous power oscillates at 2 ω. From the viewpoint of the NIC design, the improved second-order–second-order generalized integrator based on quadrature signal generation (SO-SOGI-QSG) [39], which has excellent performance in eliminating the oscillation component and implementing the designed characteristics of the SSI, is adopted here. P_e is calculated from the instantaneous measured values of voltage and current using (1) and is used as the input in Figure 3. Also, the reactive power required for voltage control is computed by (2).

$$P_e = \frac{v_\alpha^{grid} i_\alpha^{inv} + v_\beta^{grid} i_\beta^{inv}}{2} \tag{1}$$

$$Q_e = \frac{v_\beta^{grid} i_\alpha^{inv} + v_\alpha^{grid} i_\beta^{inv}}{2} \tag{2}$$

The SSI has an LVRT operation function for grid-side failures [20], but this is not modeled in this paper.

2.4. Design of the SSI Core Model

The core model, consisting of a synchronous generator Xd' model, a governor, and an AVR/AQR, is shown in Figure 4. The output voltage of the SSI is controlled by the core dynamics, which simulate the behavior of an actual synchronous machine and generate a synchronizing force. Based on this, the proposed model can improve grid damping and enable the system's stable operation with multiple SSIs.

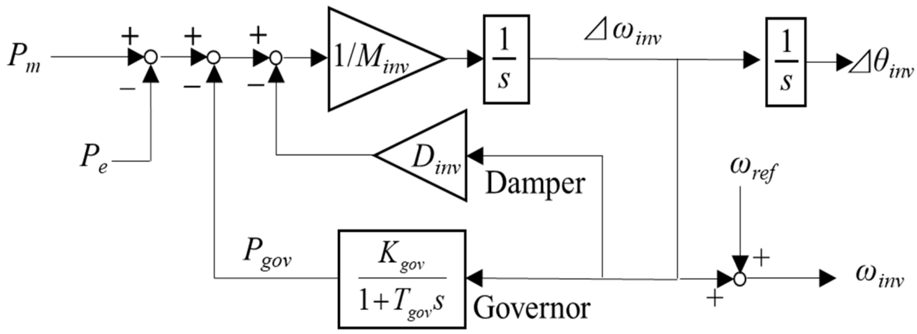

(**a**)

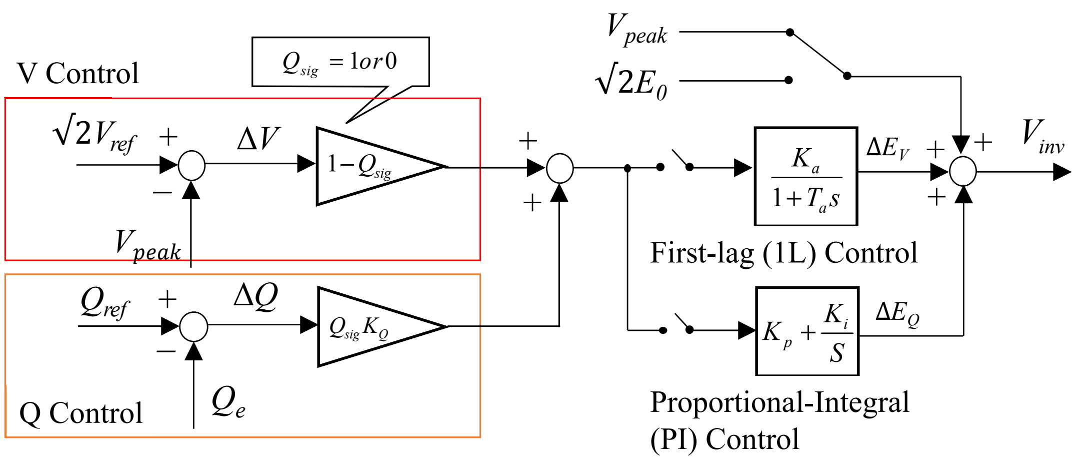

(**b**)

Figure 4. The SSI core model: (**a**) synchronous machine model and (**b**) AVR/AQR controller. Either V or Q control is selected by the value of Q_{sig}.

The conventional Xd' model, which governs the SSI EMF, is represented by the swing equation model of the synchronous machine (Figure 4a) as below.

$$M\frac{d\omega}{dt} + D\left(\omega - \omega_{ref}\right) = P_m - P_e, \quad P_m = P_{GOV} \tag{3}$$

$$\frac{d\theta}{dt} = \omega \tag{4}$$

where M is the inertia coefficient, D is the damping coefficient, P_m is the generator's mechanical input [W], P_e is the electrical output power of the generator [W], ω is the internal angular frequency [rad/s], ω_{ref} is the angular frequency reference [rad/s], θ is the internal phase angle [rad], and P_{GOV} is the governor output (where $P_m = P_{GOV}$).

A first-order delay governor is implemented, as shown in Figure 4a, in the core part. The internal frequency ω_{inv} and the pseudo-rotor angle θ_{inv} of the inverter can be obtained from this model.

The AVR, which controls the terminal voltage, and the governor, which controls the generator output, are represented by the first-order delay model in (5) and (6), respectively.

$$T_{AVR}\frac{dV_{AVR}}{dt} = -V_{AVR} - K_{AVR}\left(V - V_{ref}\right), \quad E = E_0 + V_{AVR} \tag{5}$$

$$T_{GOV}\frac{dP_{GOV}}{dt} = -P_{GOV} - K_{GOV}\left(\omega - \omega_{ref}\right) + P_s \tag{6}$$

where T_{GOV} is the governor time constant [s], K_{GOV} is the governor gain, P_s is the command value of generator operation [W], T_{AVR} is the AVR time constant [s], K_{AVR} is the AVR gain, V_{ref} is the reference voltage [V], E is the effective value of voltage [V], and E_0 is the internal voltage reference of the generator [V].

2.5. Voltage and Reactive Power Control of the SSI (AVR/AQR)

Conventional small-capacity generators follow the grid and maintain stability by controlling the reactive power by AQR. Also, large-capacity generators use AVR to control the grid voltage within the desired limits. The proposed control system for an SSI designed for MG operation is shown in Figure 4b. The SSI is designed as a GFM inverter and is operated in AQR mode during grid interconnection, which provides synchronization and inertia forces to the grid during disturbances. In this case, the reactive power reference value Q_{ref} in Figure 4b is set to 0 var, and proportional-integral (PI) control with an integrator is used to prevent reactive power output.

On the other hand, the SSI control system also needs to maintain grid voltage through AVR operation. Therefore, Q_{sig} in Figure 4b is set to 0 or 1 so that the SSI control system can be switched between the voltage control (AVR control) and reactive power control (AQR control) modes. In addition, the first-order delay system is used because the droop characteristic is necessary for the coordinated operation of multiple units. When PI is used for the parallel operation of multiple SSIs, especially in AVR operation, the SSIs will interfere and become unstable.

2.6. Inverter Model with Pseudo-Inertia

The validity of the inverter model with pseudo-inertia is verified through experiments on an actual SSI system. The model is generally equivalent to the model in (3)–(6) but differs in the following points:

- The inverter's feedback structure is slightly changed from the actual generator model for both noise reduction and performance improvement;
- The SSI utilizes an effective overcurrent suppression method without inner loops [38], where the current control is activated when the critical condition is detected. In this paper, a current limiter is used to approximate this function; however, the upper limit of the current limiter is not set in this examination.

2.7. Hardware of the SSI

Figures 5 and 6 illustrate the hardware configuration of the SSI developed in the Electric Power and Energy System Lab, Hiroshima University, Japan. The following components are used in the experimental test system:

- DC voltage source: 16 lead-acid batteries (12 V) connected in series;
- Inductor: 10 mH/3.5 Apeak, Pony Electric, Gunma, Japan;
- Nosie Filter: NAH-20-472-B, COSEL, Toyama, Japan, is inserted at the output end to prevent noise on the power supply line;
- Current sensor: MWPE-IS-03, Myway Plus Corp, Yokohama, Japan;
- Voltage sensor: a self-made sensor circuit.

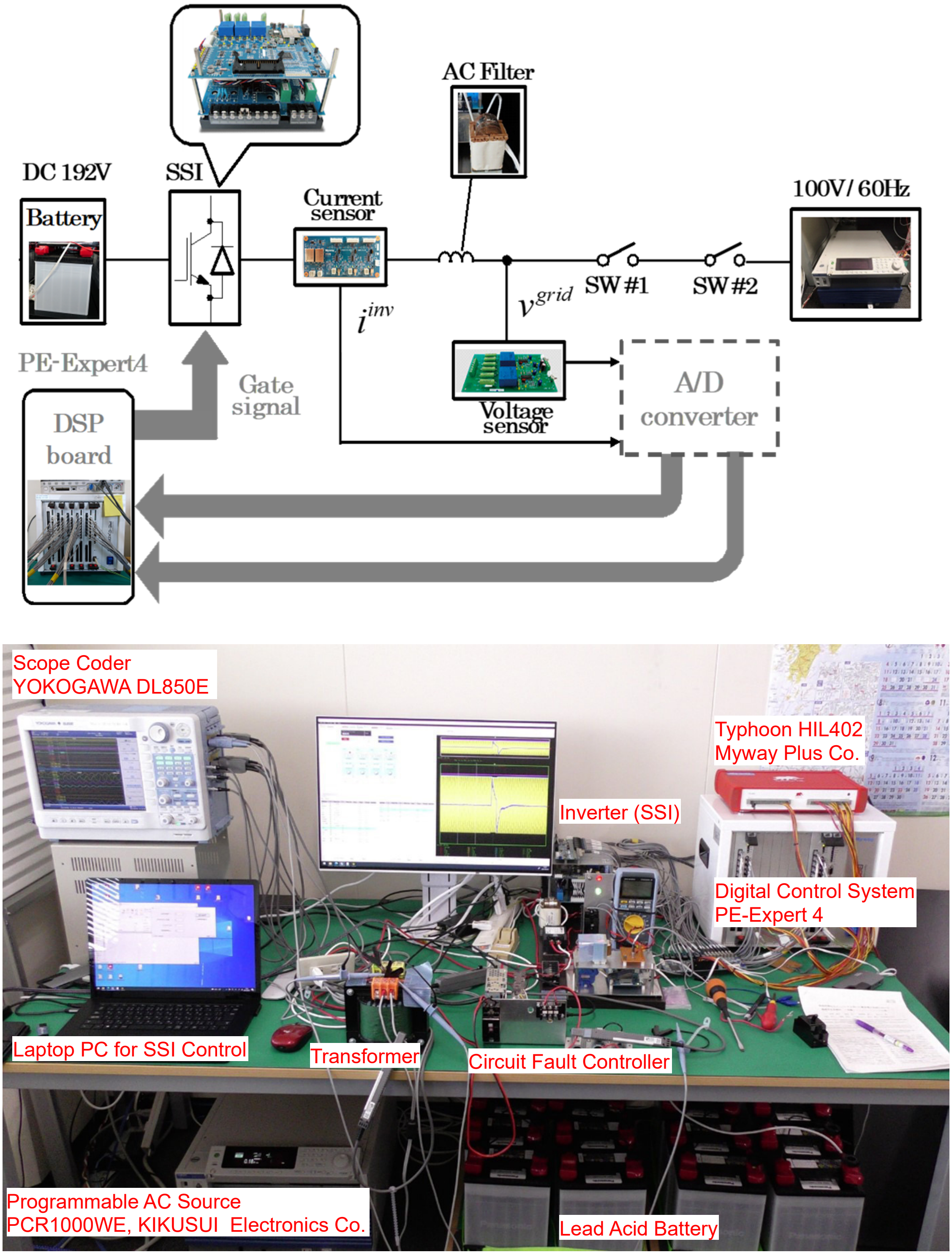

Figure 5. Experimental Setup.

The proposed control system is coded in C language and carried out on a digital signal processor (DSP) board (PE-Expert4: Myway Plus Corp).

The CPU frequency of the PE-Expert4 is 1.25 GHz, and the carrier frequency of the PWM is 20 kHz. The experimental data were measured using a Myway Plus PE-View X with a sampling frequency of 20 kHz. A grid-simulated power supply (PCR1000LE, Kikusui Electronics, Yokohama, Japan) is connected to the AC power supply side.

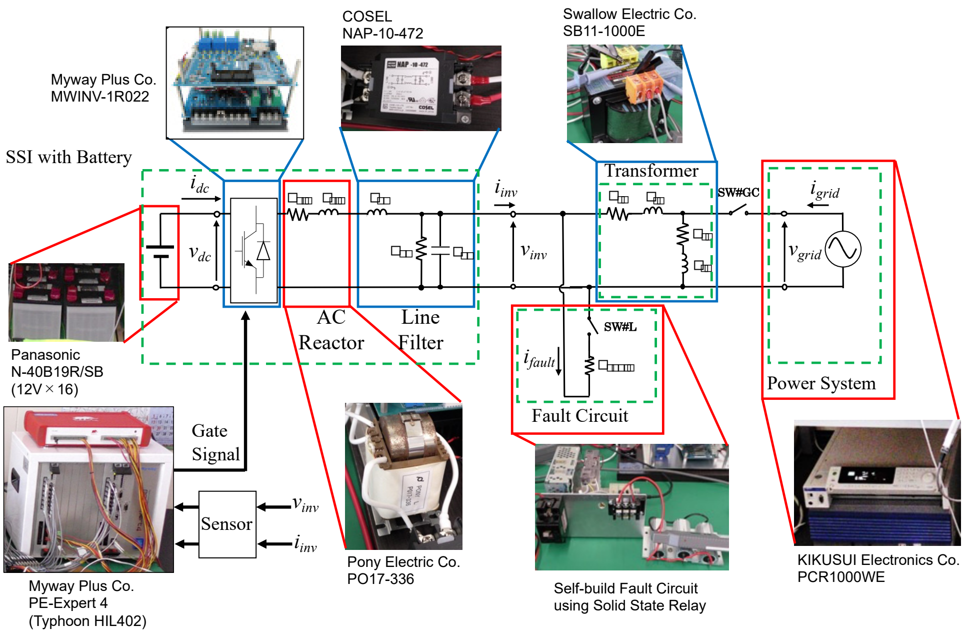

Figure 6. Experimental equipment.

3. Development and Validation of the RMS Simulation Tool

3.1. Development of the RMS Simulation Tool Based on the NIC Design

A simulation tool based on the RMS model was developed, consisting of the SSI core model, the conventional generator model, and the network model, as shown in Figure 7, using MATLAB/Simulink version 2022b. The SSI core model consists of the swing equation, AVR/AQR, and governor given in Section 2.3, which are combined with the power system network model to constitute the RMS simulation tool. The derivation of the RMS tool is based on the NIC design method in Figure 1, which is consistent with the inverter design. The RMS simulation tool can be used for conventional transient stability analysis with/without SSIs in multi-machine power systems. A large number of SSIs are modelled using the conventional theory of dynamic equivalents for parallel generators [34].

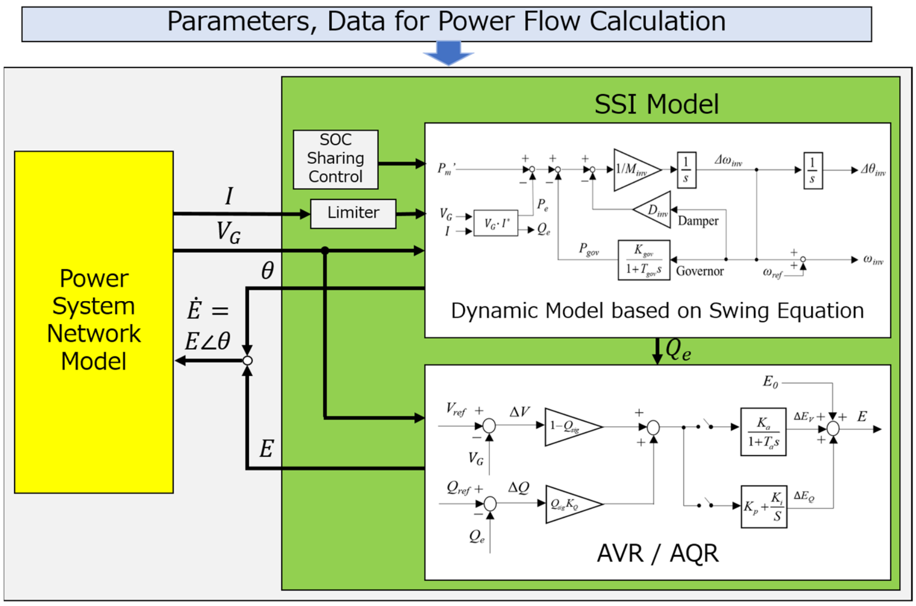

Figure 7. RMS analysis model of the SSI using MATLAB/Simulink.

The SSI is assumed to be installed to a low-voltage single-phase distribution line on the customer side, but it is also possible to configure it as a three-phase configuration and connect it to a high-voltage distribution line. This paper assumes that the SSIs are uniformly distributed across the low-voltage distribution line without three-phase imbalance.

The analysis tool is described as follows: First, the input data are the parameters for SSIs, generators, loads, and network. Then, power flow calculations are performed, and the initial state is calculated. Based on this, the RMS simulation can be performed under various conditions. The RMS model in Figure 7 was designed as a common model so that conventional generator analysis can also be performed.

The developed method is compared with the Y method, the standard tool by CRIEPI (Central Research Institute of Electric Power Industry) for transient stability analysis. It was confirmed, in a case where no SSI inverters are installed, that the computed responses of generators are almost equivalent to each other, as shown in Figure 8.

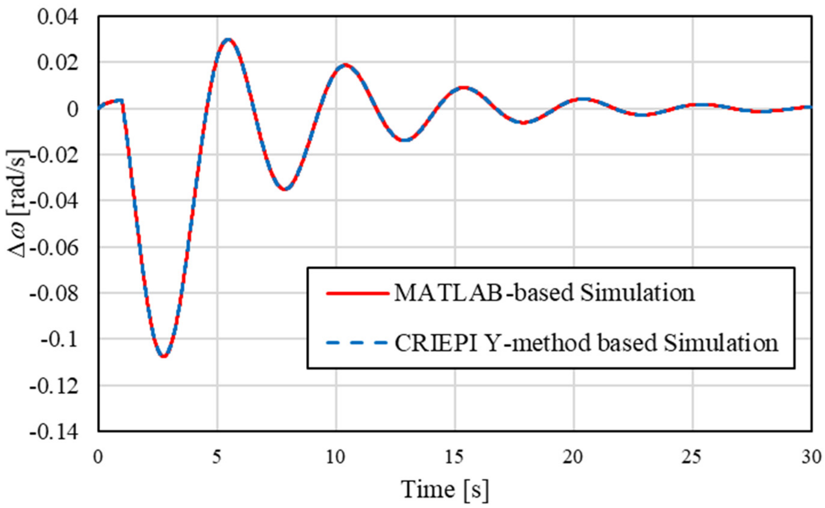

Figure 8. Comparison result (transient stability analysis tool).

3.2. Experimental System of the Grid-Connected SSI for Validation

This section describes an experimental system for investigating the validity of the developed simulation tool given in the previous section. Figure 9 shows the experimental system where the SSI is connected to the infinite bus. The system and SSI control parameters are listed in Tables 1 and 2, respectively. Note that the parameter $\widetilde{M}$ is set to a small value to realize strong damping condition for a single SSI but the optimal value is still under study. If $\widetilde{M}$ is set to a larger value, we can observe a typical transient behavior of conventional generators (see Appendix A).

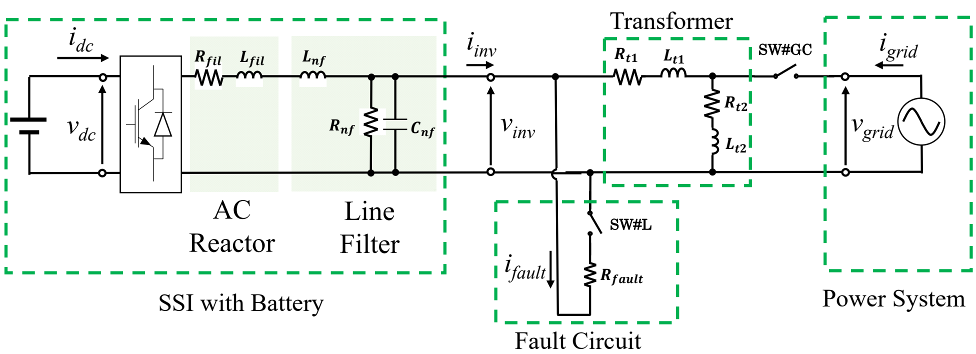

Figure 9. Experimental circuit of a single SSI connected to the infinite bus.

Table 1. Parameters in the experimental circuit in Figure 9 (Reference [34]).

Parameters	Values
R_{fil}	0.48 Ω
L_{fil}	10 mH
L_{nf}	1.4 mH
R_{nf}	470 kΩ
C_{nf}	0.95 µF
R_{fault}	100/3 Ω
R_{t1}	1.00 Ω
L_{t1}	1.48 mH
R_{t2}	43.4 Ω
L_{t2}	516.1 mH

Table 2. SSI control parameters in Figure 4 (Reference [34]).

Parameters	Values
$\widetilde{M}$ [W·s²/rad]	1 *
P_m [W]	0
ω_{ref} [rad/s]	120π
$\widetilde{D}$ (Simulink, HIL) [W·s/rad]	100
$\widetilde{D}$ (Experimental) [W·s/rad]	50 *
V_{ref} [V]	100
Q_{ref} [var]	0
Q_{sig} ("0": AVR, "1": AQR)	1
SW condition ("0" = 1 L, "1" = PI)	1
K_a	1
K_p	0
K_i	5
K_Q	0.05

* $H = 60\pi\widetilde{M}/1\ \text{kW} = 0.188$ [s], $D = (\omega_0/1\ \text{kW}) \times \widetilde{D} = 18.85$ [pu].

A short-circuit fault was applied to a grid connection line through a fault resistance, started at 0.4 s until 0.5 s, when the fault is cleared. This was carried out by the fault circuit in Figure 9 in which variable fault timing can be set. Two cases of fault timings were adopted, these being 0° and 90° from the zero-cross detection of the terminal voltage, which, respectively, correspond to the minimum and maximum timing of voltage disturbances. In this situation, actual hardware experiments were carried out.

Then, the HIL simulations and RMS simulations were conducted. In the HIL simulations, the changes in the phase conditions for fault occurrence and clearance were not considered. Instead, the pre-set phase condition approximately 9° from the zero-cross detection was used for the convenience of the simulation.

3.3. Comparison between Experiments, HIL, and RMS Simulations

In order to investigate the effect of fault timing (phase condition) on SSI behavior, the transient waveforms were observed by changing the fault timing every 10°. As expected, the transient waveform of P_e after the fault was almost the same. Table 3 shows the quantitative evaluation of the transient waveform in terms of the fault timing and the maximum power value. It was noticed that the fault timing (phase condition) has almost no effect on the RMS value.

Table 3. Response of Pe [W] (RMS value).

Fault Timing		Fault Duration Time	P_e [W] (Maximum RMS)
[°]	[s]		
0	0.4160	0.0160	50.51
10	0.4158	0.0158	52.73
20	0.4153	0.0153	52.61
30	0.4147	0.0147	50.40
40	0.4142	0.0142	49.65
50	0.4136	0.0136	48.08
60	0.4133	0.0133	50.79
70	0.4123	0.0123	45.30
80	0.4205	0.0205	45.97
90	0.4201	0.0201	47.06
100	0.4197	0.0197	48.74
110	0.4194	0.0194	50.24
120	0.4189	0.0189	50.08
130	0.4186	0.0186	51.69
140	0.4179	0.0179	52.02
150	0.4177	0.0177	52.68
160	0.4173	0.0173	53.06
170	0.4167	0.0167	53.70
180	0.4161	0.0161	51.93

Figures 10 and 11 show the results of the experiments, HIL (9° of fault timing), and RMS simulations for the extreme cases corresponding to 0° and 90° fault timings, respectively. The comparison of the instantaneous waveform P_e (Figure 10c) for the HIL simulation and the experimental results shows that they are almost equivalent to each other. The difference comes from the preset switching timing of fault occurrence and clearance in the HIL device. The comparison shows that although the shock immediately after the fault differs depending on the fault timing, the values are close to each other regardless of the different fault timings.

Figures 10e and 11e show the mean values of the P_e output of the SSI, which are obtained by the SSI hardware, compared with those obtained by the HIL simulation (9°) and the developed RMS simulation model. It was observed that they agree with each other, implying that all of those simulations are successfully approximate the experimental waveforms. The HIL simulation result is not shown in Figure 11e since there is no corresponding case, as mentioned before.

Figures 10f and 11f present the same as Figures 10e and 11e with different time scales, where the instantaneous values of P_e, and their mean values given by different filters are added. It is noted that the filter outputs show delays in the P_e response since the mean value of P_e is defined by the following equation, which must include the delays of the half-cycle of P_e oscillations: 0.01 s.

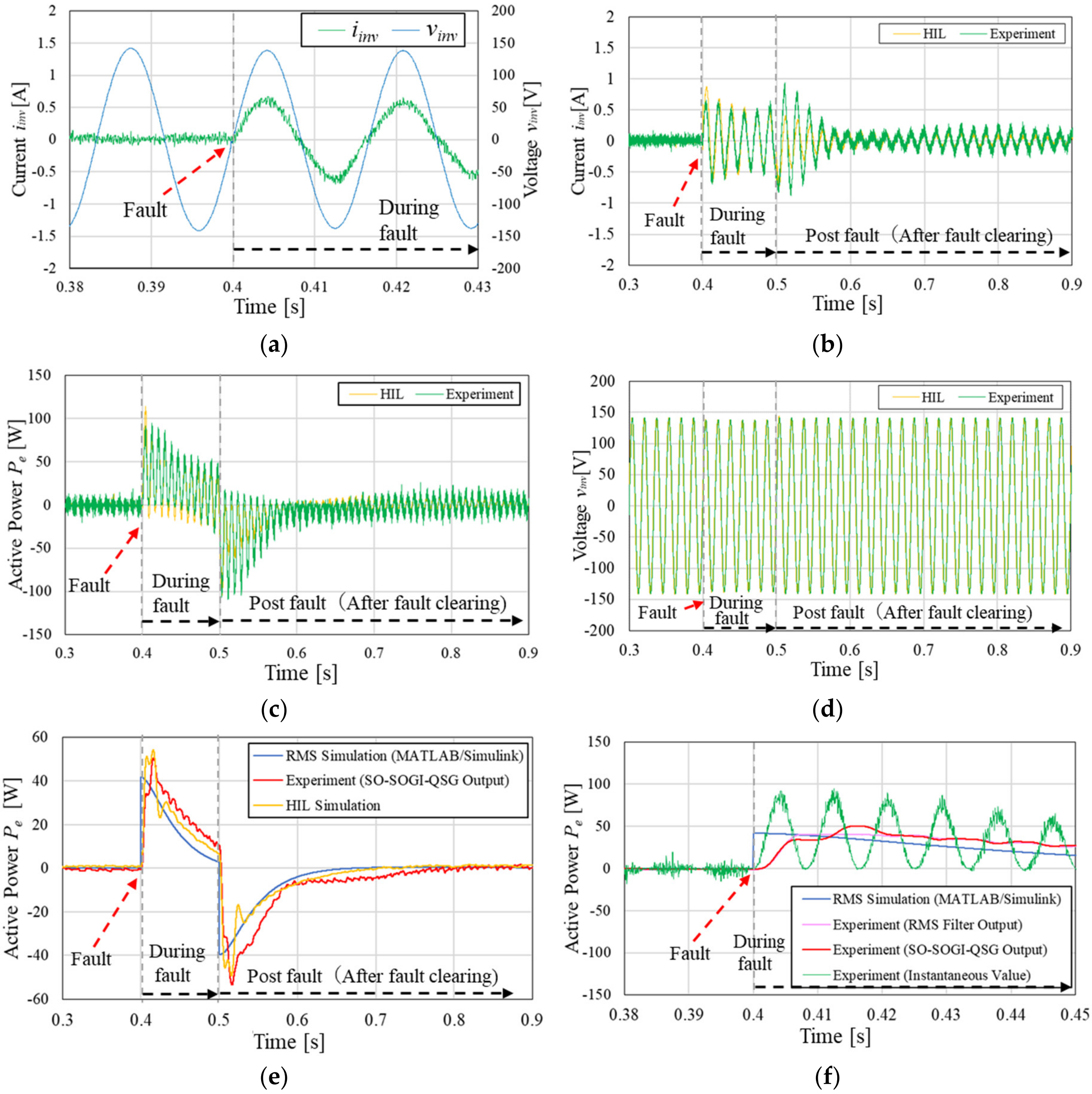

Figure 10. Comparison between the experimental study and simulation for a 0° fault timing: (**a**) output current [A] and voltage [V] of the SSI; (**b**) output current of the SSI [A] (instantaneous value); (**c**) active power P_e of the SSI [W] (instantaneous value); (**d**) output voltage of the SSI [V] (instantaneous value); (**e**) active power P_e of the SSI [W] (mean values); (**f**) active power P_e of the SSI [W] (instantaneous and mean values).

$$\begin{aligned} P_e &= \frac{1}{T}\int_{t-T}^{t} (i_{inv}(t) * v_{inv}(t))dt, T = \frac{1}{2*60} \\ &\cong \frac{1}{T} * \sum_{n=t-T}^{t} \frac{1}{2} * \Delta t * (P_{en+\Delta t} - P_{en}),\ \Delta t = 0.00002 \end{aligned} \tag{7}$$

On the other hand, the instantaneous waveforms of P_e outputs exhibit almost no delays since the internal voltage of the GFM, as a constant voltage source, instantly supplies current and power based on Kirchhoff's law, depending on the grid-side conditions. The quick responses of the SSI hardware are successfully approximated by the RMS simulation model (MATLAB/Simulink). It was observed that the mean value of P_e was identical for the different fault timings, while the transient waveform of P_e after the fault was also not much affected by the fault timings, as expected. It was noted that the experimental results were affected by the noise suppression elements used, while the RMS simulation does not consider these elements.

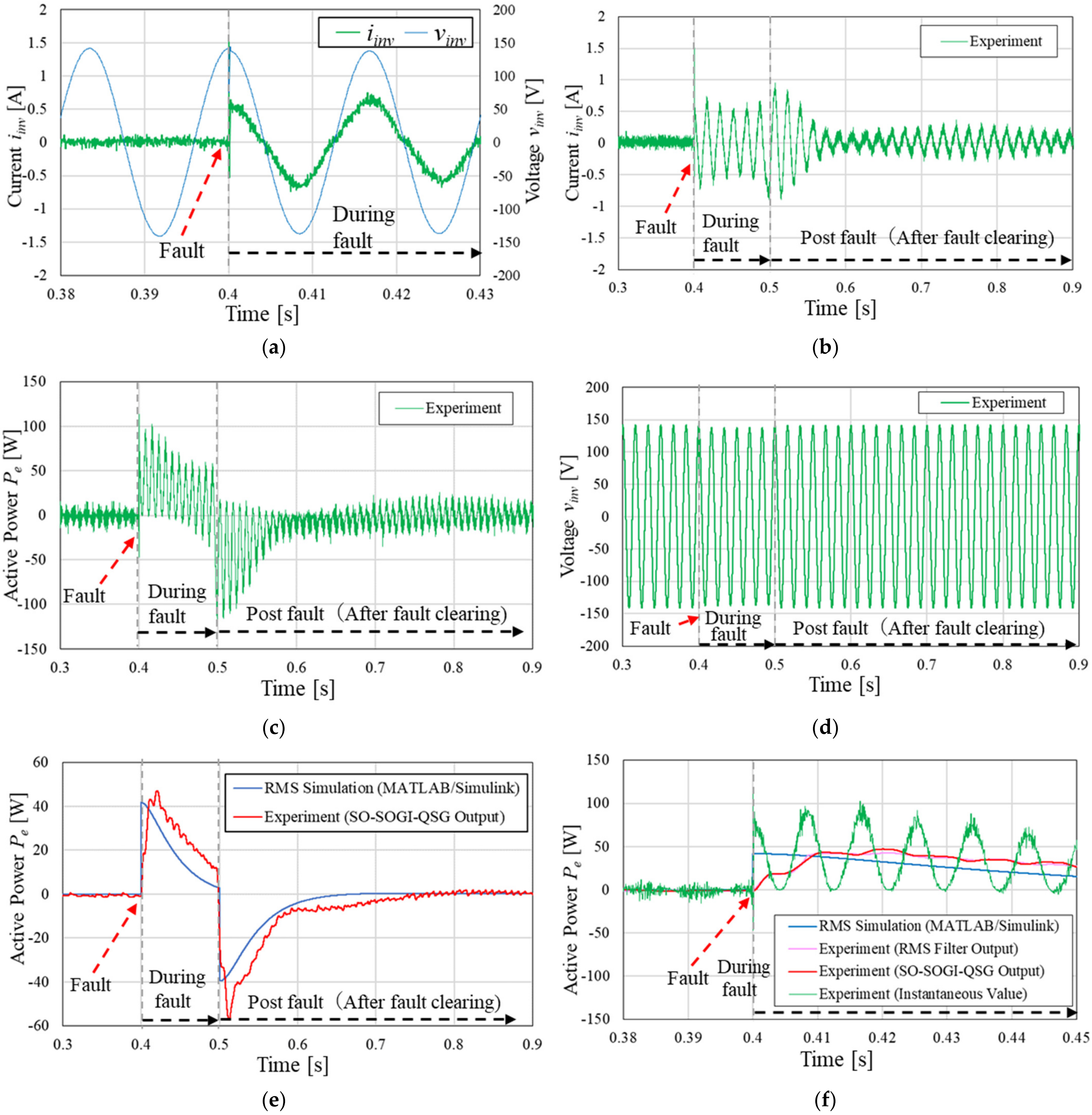

Figure 11. Comparison between the experimental study and simulation for a 90° fault timing: (**a**) output current [A] and voltage [V] of the SSI; (**b**) output current of the SSI [A] (instantaneous value); (**c**) active power P_e of the SSI [W] (instantaneous value); (**d**) output voltage of the SSI [V] (instantaneous value); (**e**) active power P_e of the SSI [W] (mean values); (**f**) active power P_e of the SSI [W] (instantaneous and mean values).

Figure 12 shows the results of the MATLAB/Simulink RMS simulation models with and without the effect of the measurement devices, including noise filters. It can be confirmed that the results are almost the same.

From the investigations in this section, we can confirm the validity of the developed RMS simulation tool, which provides enough accuracy to analyze power system transient behavior. The error in the active power waveform is about 10% when observing Figure 10e.

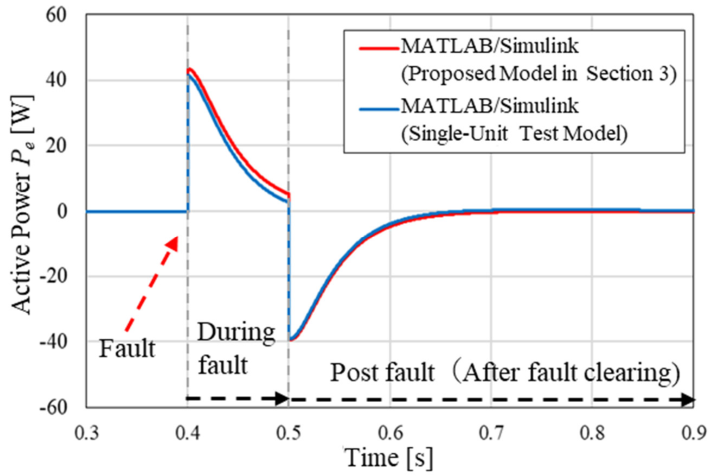

Figure 12. Active power P_e of the SSI obtained by RMS simulations.

4. Power System Stability Evaluation

4.1. Case Setting for Stability Assessment

The RMS simulation model is used to analyze a power system in which multiple conventional generators and SSIs are operated. The stability analysis of the power system with IBRs and conventional generators was performed using the Anderson–Fouad nine-bus system shown in Figure 13, where photovoltaic power generators (PVs) and an SSI are installed at bus 5. The SSIs are connected to the low-voltage distribution system through the impedance of the distribution lines and distribution transformers, as shown in Figure 14. A large number of SSIs connected to bus 5 are represented as an equivalent single SSI model as mentioned before. The stability evaluation methods are summarized in Table 4. Study cases are given in Table 5, where the 60% of the original conventional generation in Case 1 is replaced by PV generation in Cases 2–4. The output power reduction in the conventional generators in these cases is given in Figure 15b, in which three of the five units are out of service. The conditions in Figure 15a is not used in this paper. Thus, the system inertia was also reduced by 60% in Cases 2–4. The operating conditions of the SSI (VRE) installation cases are also given in Table 5, and are described below.

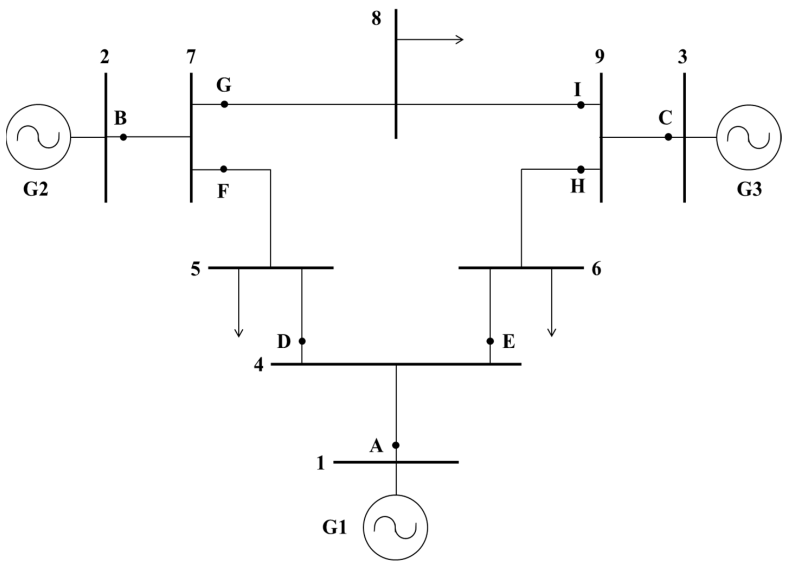

Figure 13. Anderson–Fouad nine-bus three-generator system. G1 to G3 represent conventional generators. Numbers 1 to 9 stand for nodes (buses). A to I are fault locations. Arrows represent loads where PVs and SSIs are installed.

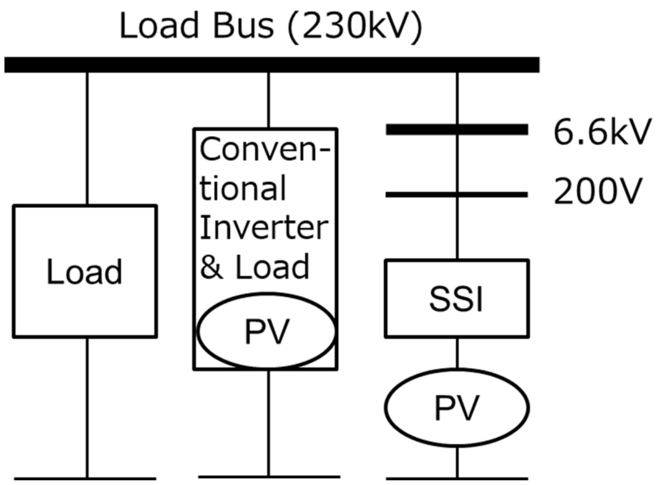

Figure 14. The installation of SSIs.

Table 4. Stability evaluation method.

Disturbance	Stability	Evaluation Indices
Generator Outage	Frequency Stability Small-Signal Stability	RoCoF, Frequency Nadir Eigenvalues
Three-Phase Ground Fault	Transient Stability Small-Signal Stability	Generator Swings Eigenvalues

Table 5. Study cases for operating condition.

Case	Total Generator' Output [%]	Total PV Output [%]	
	(G1 + G2 + G3)	Conventional Inverters	Proposed SSIs
Case 1	100	0	0
Case 2	40	60	0
Case 3		30	30
Case 4		0	60

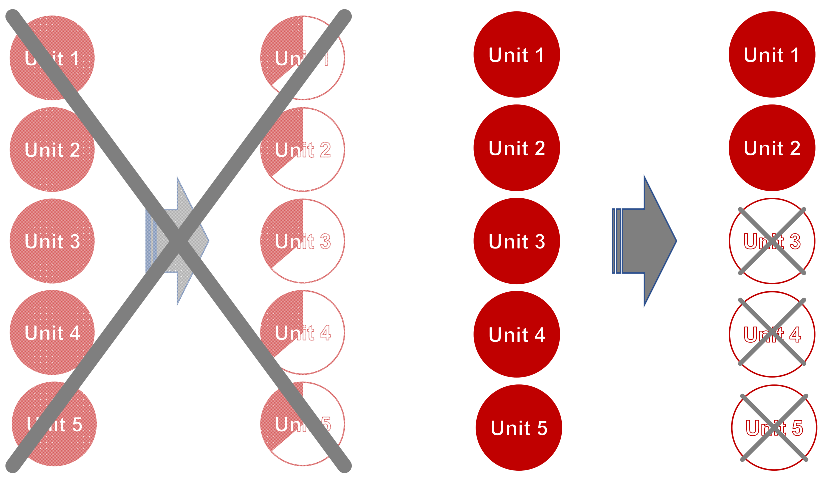

(**a**) (**b**)

Figure 15. Treatment of the system inertia: (**a**) Maintained system inertia; the condition is not used. (**b**) Reduced system inertia; the condition in this paper.

Case 1: Represents the base condition of the test system in [40] where the total power is generated from the three conventional generators without any PV installations.
Case 2: The PV penetration is 60% of the total power generation using conventional grid-following (GFL) inverters.
Case 3: Half of the conventional GFL inverters of Case 2 are replaced by SSIs, which corresponds to about 80,000 SSIs of 1 kW.
Case 4: All PV inverters are SSIs, about 160,000 SSIs.

It is assumed that the maximum output of SSIs is greater than 1 kW to stabilize the system in a transient state.

In the latter sections, the effect of the SSIs is investigated for the following events using the developed RMS simulation tool.

[Generator Outage]

It is assumed that Generator 1 consists of two units and an outage of one unit occurs at time 0 s. In order to investigate the frequency stability after the outage, the inertia center frequency of the three generators is evaluated by the rate of change of frequency, RoCoF, and the frequency nadir. The RoCoF is defined as the maximum value of frequency change up to 1 [s] after the disturbance. The frequency nadir is the maximum deviation from 60 [Hz] after the disturbance.

[Three-Phase Ground Fault]

A three-phase ground fault is assumed in one of the two transmission lines at point F. The fault is cleared after 0.01 s, and the transient stability of the generator is examined. The parameter settings of the generators and SSIs are shown in Table 6.

Table 6. Simulation parameters.

Parameters	Generators and SSI			
	G1	G2	G3	SSI(/Machine)
Rated Capacity	247.5 [MVA]	192.0 [MVA]	128.0 [MVA]	1 [kVA]
H [s]	23.64	6.4	3.01	9.42
D [p.u.]	2.0	2.0	2.0	37.7
x_d' [p.u.]	0.0608	0.1198	0.1813	0.4298
K_{GOV}	0.0663	0.0663	0.0663	0.1
T_{GOV} [s]	1.0	0.5	0.5	0.02
K_{AVR} [s]	0.1	0.1	0.1	0.1
T_{AVR} [s]	0.5	0.5	0.5	0.5

4.2. Frequency Stability Evaluation against Generator Trip

The simulation results for the generator outage are shown in Figure 16. From this figure, it can be observed that the grid frequency response improves as the number of SSIs installed increases. The inertia center frequency is shown in Figure 17, and the characteristic index values obtained from it are shown in Table 7 and Figure 18. In Case 1, before the introduction of PVs, the frequency change was small. However, in Case 2, the frequency change was very large after PV installation. In Case 3, where the SSI was used, a significant improvement was observed. In Case 4, where all inverters are replaced by SSIs, the frequency characteristic was improved furthermore to an original level without PVs. The same effect can be demonstrated by the active power output shown in Figure 19.

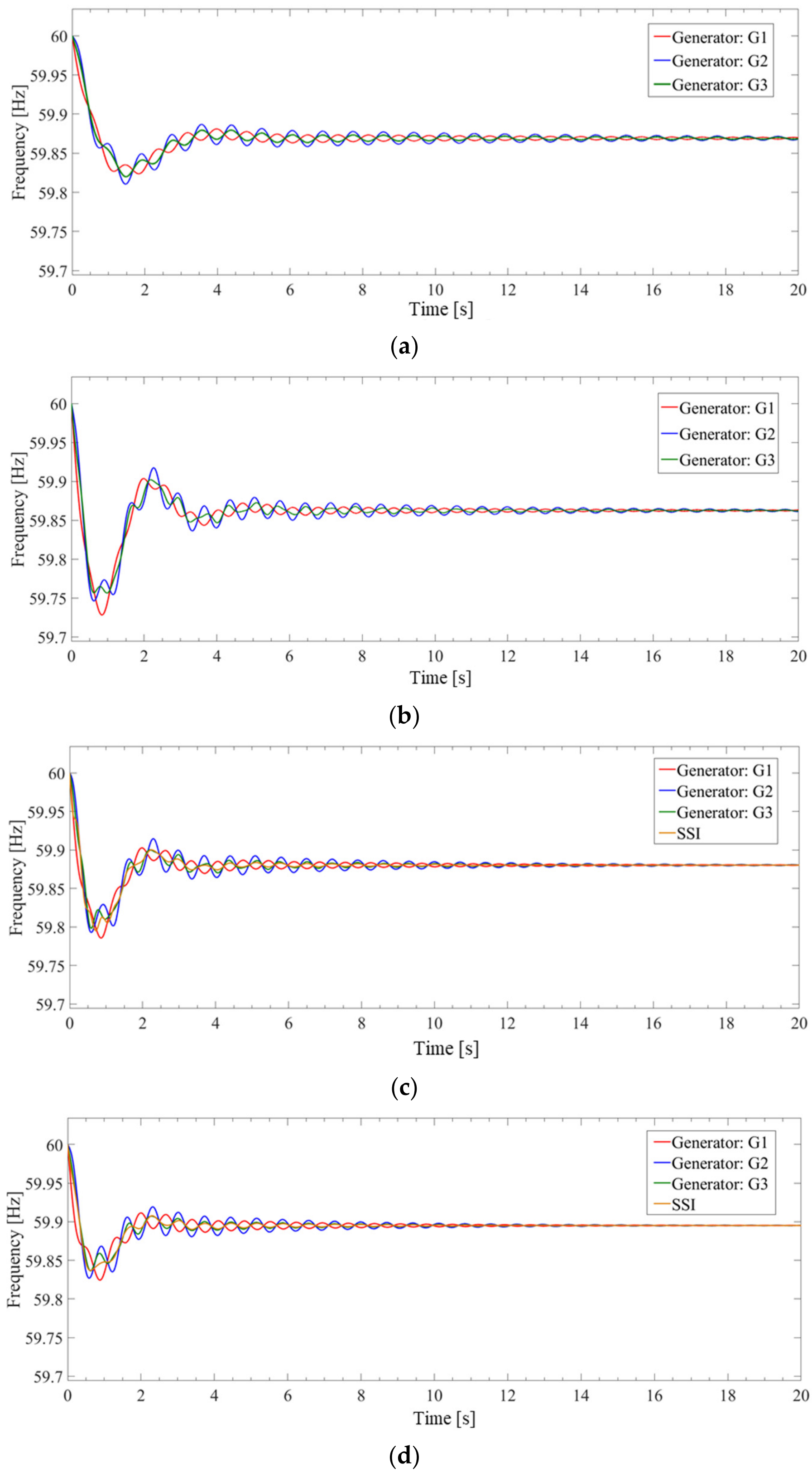

Figure 16. System frequencies after generator outage: (**a**) PV = 0 [%], SSI = 0 [%] (case1); (**b**) PV = 60 [%], SSI = 0 [%] (case2); (**c**) PV = 60 [%], SSI = 30 [%] (case3); (**d**) PV = 60 [%], SSI = 60 [%] (case4).

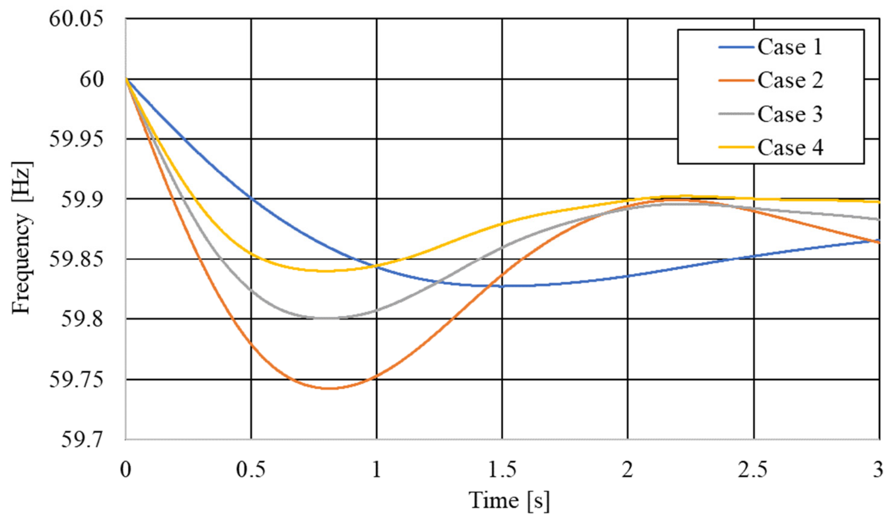

Figure 17. Comparison of inertia center frequency.

Table 7. Frequency nadir and RoCoF.

Cases	Nadir [Hz]	RoCoF [Hz/s]
Case 1	−0.173	−0.222
Case 2	−0.258	−0.551
Case 3	−0.199	−0.472
Case 4	−0.160	−0.413

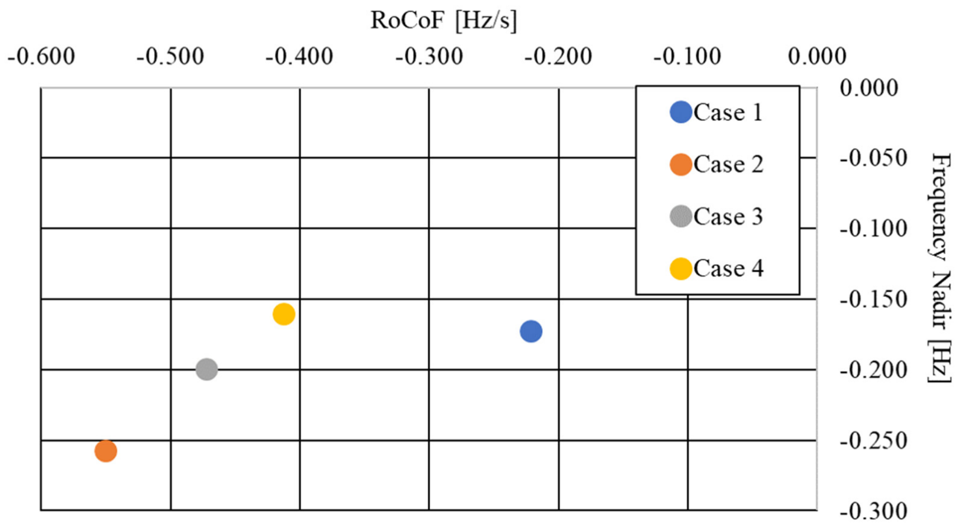

Figure 18. Plots of RoCoF against frequency nadir.

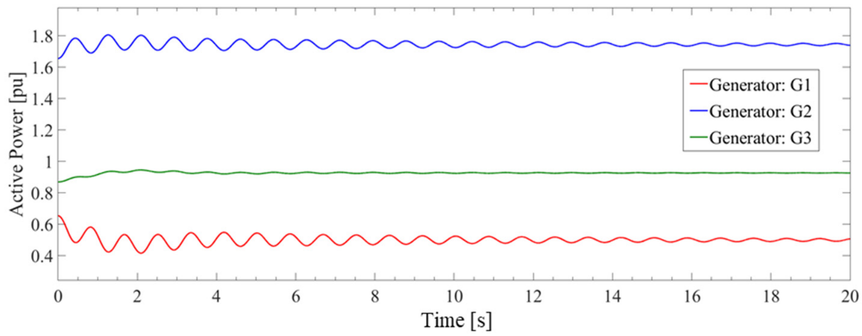

(**a**)

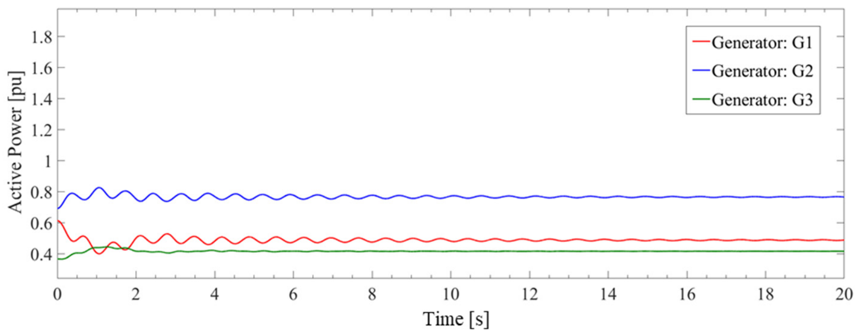

(**b**)

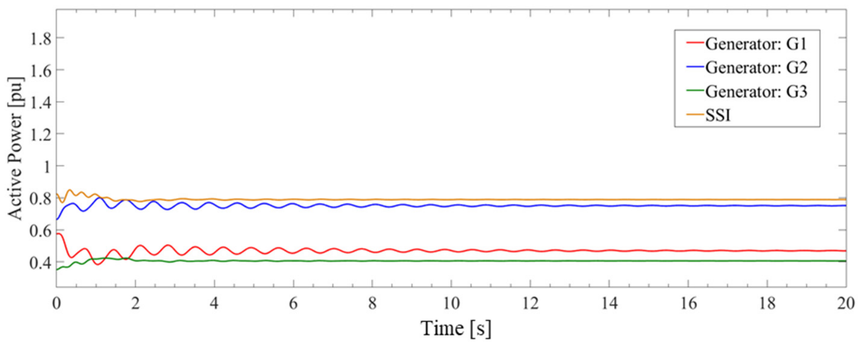

(**c**)

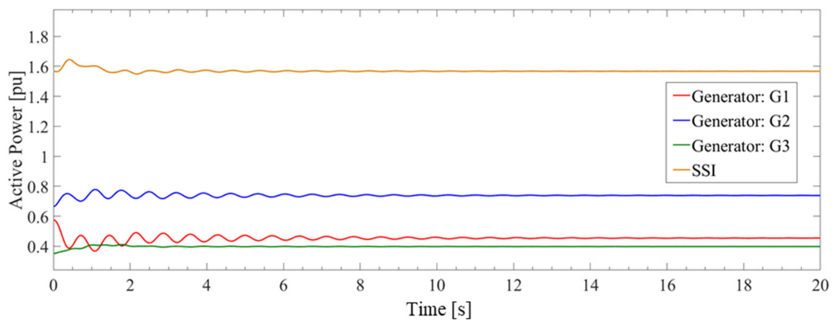

(**d**)

Figure 19. Power outputs after generator outage (100 MVA base): (**a**) PV = 0 [%], SSI = 0 [%] (case1); (**b**) PV = 60 [%], SSI = 0 [%] (case2); (**c**) PV = 60 [%], SSI = 30 [%] (case3); (**d**) PV = 60 [%], SSI = 60 [%] (case4).

4.3. Transient Stability Evaluation for a Three-Phase Ground Fault

Figure 20 shows the generators' frequencies at the time of a three-phase ground fault. From the figure, it can be observed that the transient stability of the system is improved in Figure 20b due to the light load condition even for the conventional inverters. Further stabilization is observed in Figure 20c,d as the number of SSIs increases, which demonstrates the stabilizing effect of the SSIs.

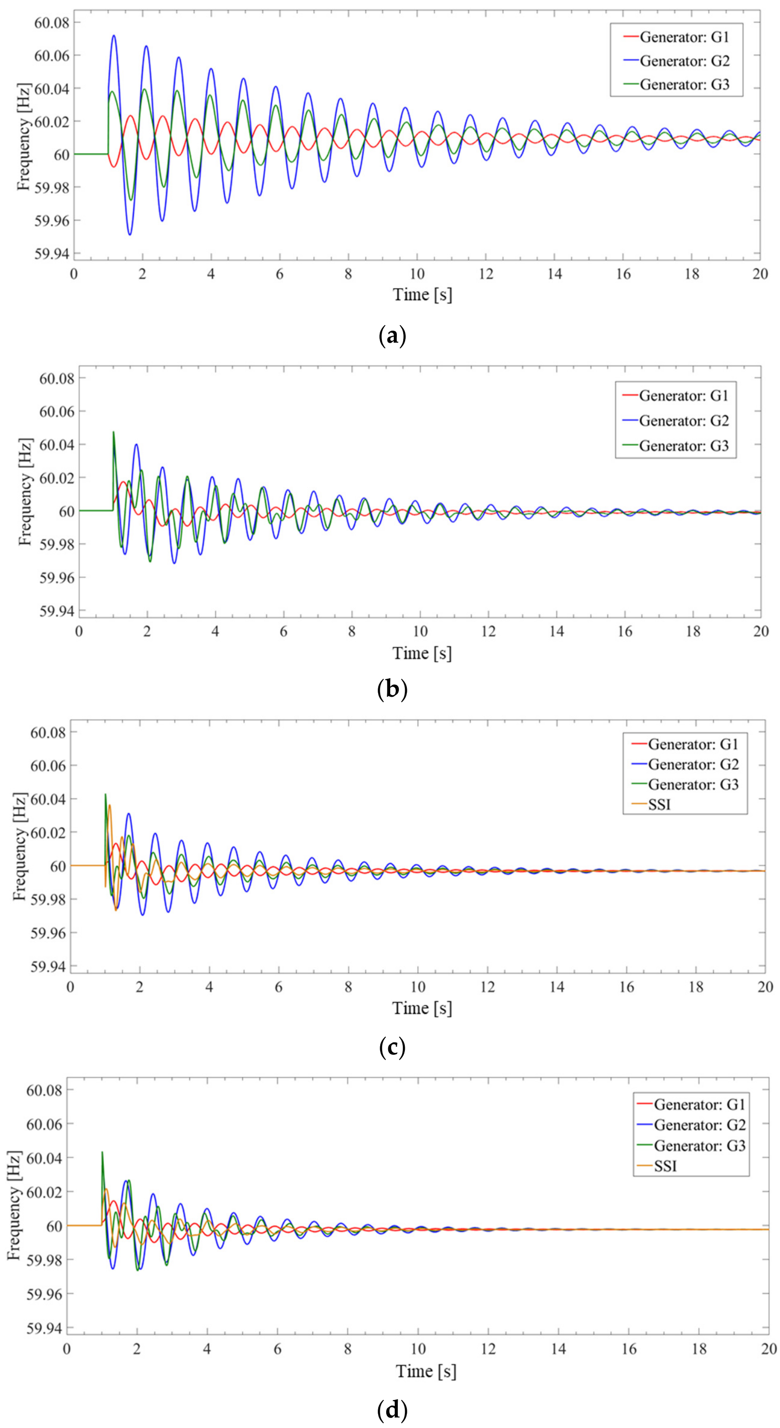

Figure 20. Generator swings (3 LG at F, CT = 0.01 [s]): (**a**) PV = 0 [%], SSI = 0 [%] (case1); (**b**) PV = 60 [%], SSI = 0 [%] (case2); (**c**) PV = 60 [%], SSI = 30 [%] (case3); (**d**) PV = 60 [%], SSI = 60 [%] (case4).

4.4. Small-Signal Stability Evaluation

Figure 21 shows the eigenvalues of the conventional generators with controllers for the simulated cases for the operating conditions before disturbance, after the generator trip, and after the three-phase ground fault clearance. These results show that the SSI has greatly improved the small-signal stability of the power system for all those cases.

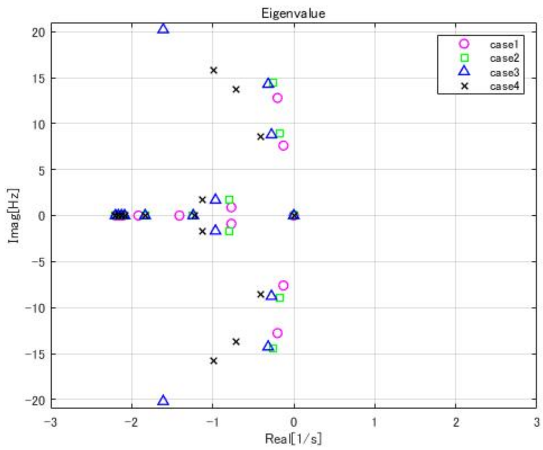

(**a**) Normal operating condition

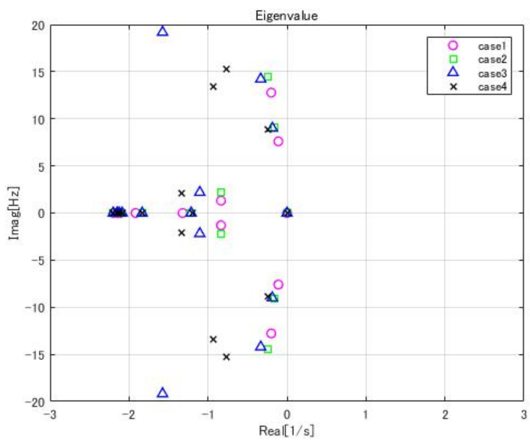

(**b**) After generator trip

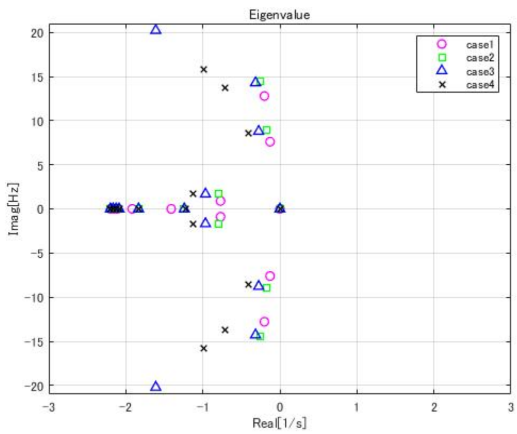

(**c**) After 3 LG fault clearing

Figure 21. Generator swings (3 LG at F, CT = 0.01 [s]).

In summary, it is confirmed that the introduction of SSIs is very effective in terms of frequency stability, transient stability, and small-signal stability. Also, introducing a large number of SSIs improves stability to a similar or even higher level than the state before the installation of PVs.

5. Effective Design of the SMG Using the SSI

5.1. Design Concept of the SMG Using the NIC-SSI

This section describes the summary of our previous works on SMGs, which includes the conceptual planning of an SMG in our project based on the proposed NIC-SSI design. In general, since the three-phase synchronous generators cannot be connected to the single-phase distribution system, it was difficult to construct a stable and reliable SMG. In this situation, the developed SSI created the possibility of constructing an SMG reliably in a low-voltage distribution system. By combining the characteristics of the proposed SSI and the storage devices of the households, various benefits can be expected, as shown in Figure 22. The proposed SMG was designed to work flexibly in normal and emergency states as follows.

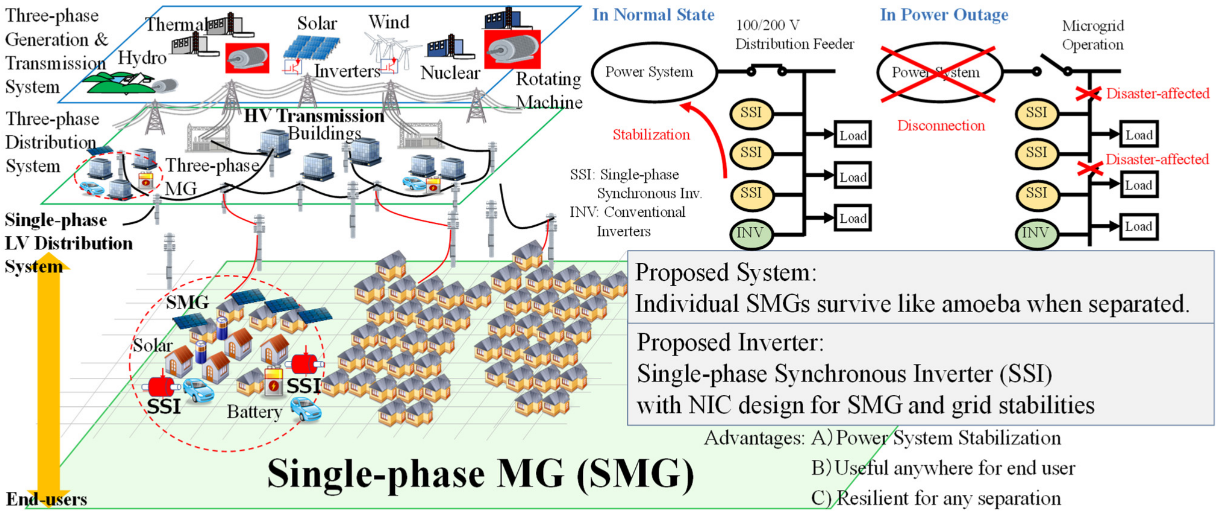

Figure 22. A 100/200 V single-phase microgrid.

[Normal State]

Currently, the number of IBRs has grown significantly, and the mechanical inertia is reduced, which leads to instability problems in the bulk power system. As was shown in the previous section, frequency stability is the main issue caused by the low system inertia, which can be considerably improved by the proposed SSI, as can the transient stability and small-signal stability. This implies that, in the normal state, the SMG with the proposed SSIs connected to the main grid provides grid stabilization effectively.

[Emergency State]

Recently, the number of power outages caused by natural disasters worldwide has increased, and MGs are considered an effective solution for recovery in various places. In such emergency cases, the construction of small-scale MGs in low-voltage distribution systems is considered effective in terms of cost and performance. Therefore, large investments and infrastructure restructuring can be avoided, which can be a truly effective solution. The basic dynamic characteristics are briefly described below.

An important point in the construction of the SMG in Figure 22 is that no major elements other than SSIs are necessary, SSIs are installed on demand side by replacing the conventional inverters for PVs, batteries, etc. Furthermore, no special operation costs are necessary in terms of grid operation since SSIs work as demand side devices, where no controls are required from the network operator. This implies that no major costs are required either in the normal state, nor in the emergency state. This is a big difference compared with usual MG schemes which require a large amount of cost expenditure for the system control devices such as large controllable generators and energy management systems (EMSs), etc., which are similar to the case of a conventional power system.

5.2. Experimental Examinations of SMG Operations

A brief explanation for the control scheme of SSIs is given using an example SMG system in Figure 23, whose experimental system is shown in Figure 24. Table 8 shows the basic control modes for SSI operations. Cases C and O correspond to close and open for the grid connection switch, SW#GC in the MG circuit diagram, Figure 23. The case number indicates the number of interconnected SSI units. For example, C1 implies that SW#GC is closed and that one SSI is connected to the grid. The control mode indicated as V-1L is for voltage control with a first-order delay and Q-PI control represents the case of reactive power control with PI control; in Case C1 (grid-connected operation), the Q-PI control is used where no reactive power is injected; in Case O1 (stand-alone operation), V-1L control is used to control the voltage; and in Case O2 (MG operation), SSI#1 operates with Q-PI control and SSI#2 with V-1L control.

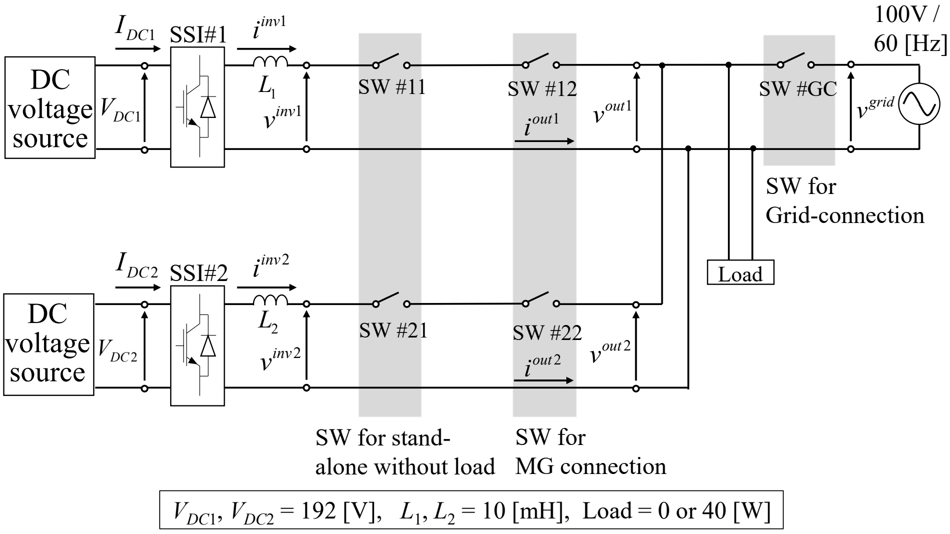

Figure 23. Circuit configuration of the SMG.

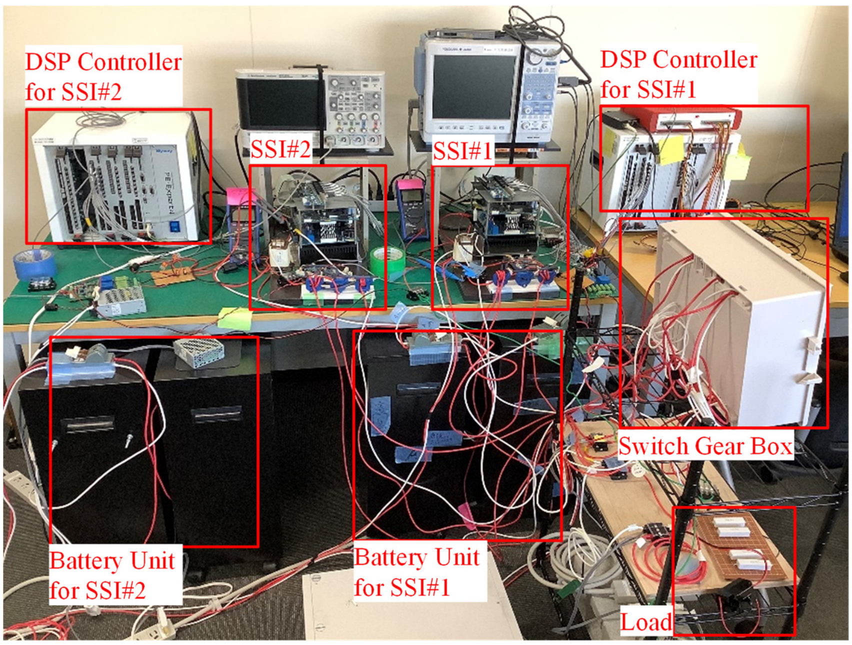

Figure 24. Laboratory experiments with two SSIs.

Table 8. Operation mode.

	Operation Mode	SW #11	SW #21	SW #12	SW #22	SW #GC	Control Mode
Case C0	In a normal state	×	×	○	○	○	
Case O0	In a power outage	×	×	○	○	×	
Case C1	SSI#1 grid-connected operation	○	×	○	○	○	SSI#1: Q-PI
Case O1	SSI#1 stand-alone operation	○	×	○	○	×	SSI#1: V-1L
Case O2	SSI#1&#2 off-grid operation	○	○	○	○	×	SSI#1: V-1L SSI#2: Q-PI

○: closed, ×: open.

5.2.1. Dynamic Performance of the SMG in Grid Connected (C0) and Stand-Alone (C1) Operations

This case simulates the switching process from grid-connected mode to stand-alone operation in case of a disaster:

t = 0 [s]:	- -	Close all switches except SW#21 Start SSI#1 under Q-PI control to synchronize with AC system.
t = 15 [s]:	-	Change SSI#1 to V-1L control mode.
t = 25 [s]:	-	Open SW#GC and allow SSI#1 to operate independently.
t = 40 [s]:	-	Apply 40 [W] to Load.

In Figure 25, SSI#1 is connected to the grid at time t = 0.0 s. The SSI#1 is synchronized with the AC system, and the output voltage is adjusted where there is no reactive power output by Q-PI control. At t = 25 s, the SSI operates independently providing active power to the local load, keeping zero reactive power output.

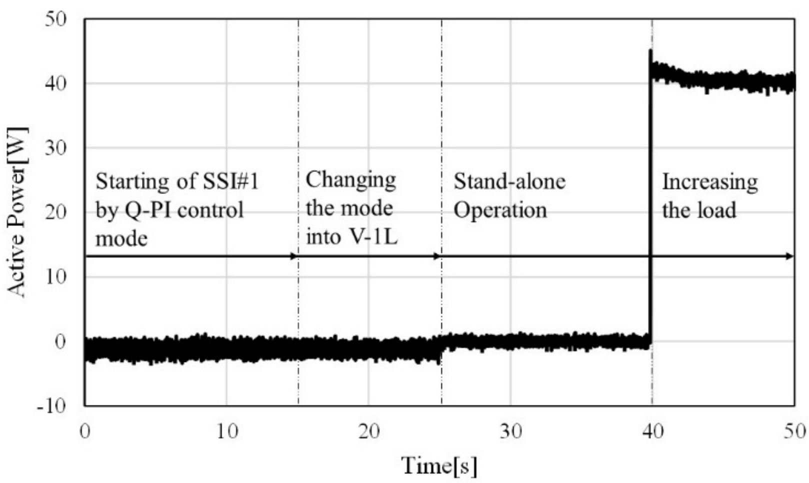

(**a**)

Figure 25. *Cont.*

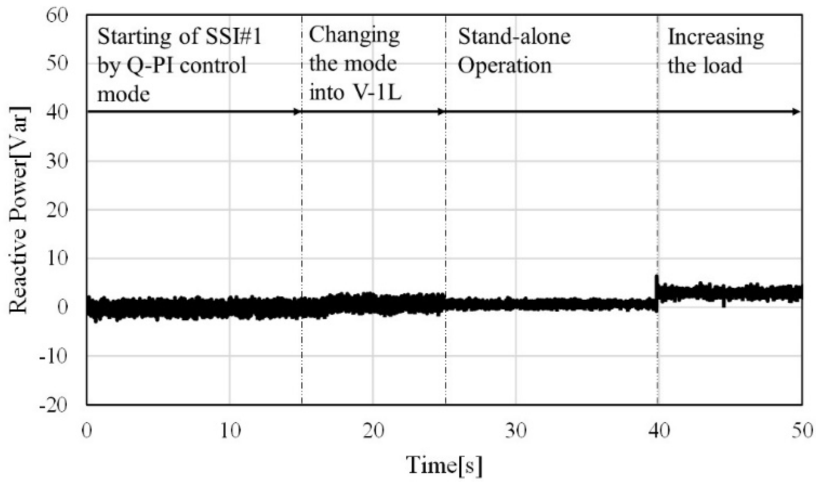

(**b**)

Figure 25. Results of experiment 1: (**a**) active power and (**b**) reactive power.

5.2.2. Dynamic Performance of the SMG in Stand-Alone (C1) to SMG (O2) Operations with Power Exchange between the SSIs

This case represents energy transfer between end-users in SMG operations during a disaster.

t = 0 [s]:	- Close SW#21. - Start SSI#2 under Q-PI control mode. - Perform MG operation using two SSIs.
t = 25 [s]:	- Set P_{m1} of SSI#1 to 100 [W]. - Set P_{m2} of SSI#2 to -100 [W]. - Transfer power between SSI#1 and SSI#2.
t = 35 [s]:	- Apply 40 [W] to Load.

Figure 26a shows that the active power is exchanged from SSI#1 to SSI#2, which implies that the SSIs can cooperate to achieve the stable operation of the SMG. Since it was confirmed that the basic characteristics of the MG frequency are equivalent to the simulated performance of the core dynamics, improved frequency control is being implemented to the SSI at present.

Although not shown, it has been also confirmed that the voltage and the current are stable, and the frequency is maintained during the operation. The response of the SSI is almost equivalent to the synchronous generator. Thus, the SSIs successfully constitute a stable SMG with good performance.

5.3. Experimental Examinations of SMG Operations with Ill-Conditioned Loads

This section examines the feasibility of SMG operations under extreme load conditions, performed in Kure KOSEN College. The following two experiments were conducted to study the performance of the SMG. One is a grid-connected SMG operation where we checked the basic performance of the SMG. The other is off-grid SMG operation which tends to be less stable compared with grid-connected operation. Therefore, its stability is an important issue in the case with poor-quality loads. Then, the stability and the performance of SMG were studied for various kinds of loads.

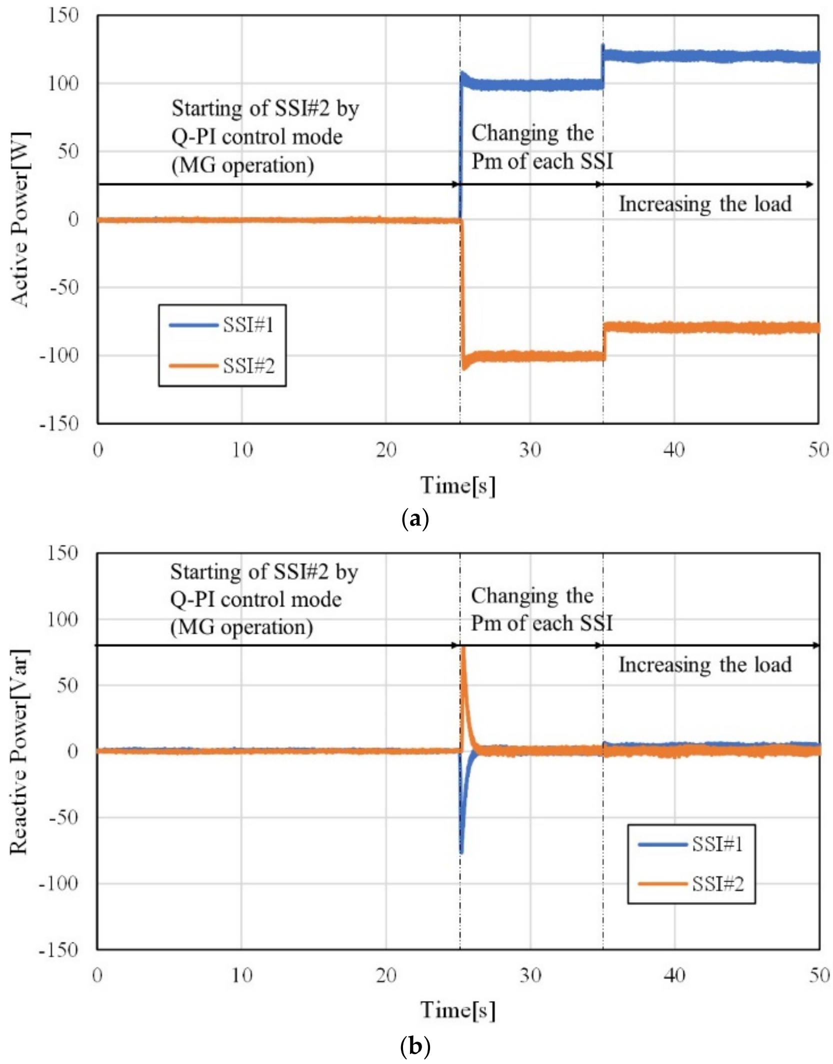

Figure 26. Results of experiment 2: (**a**) active power and (**b**) reactive power.

Figure 27 shows the experimental environment. The circuit used in the experiment consists of two SSI units, a grid-simulated power supply and a load, as shown in Figure 28 and Table 9. In this experiment, 16 lead-acid batteries (12 [V]) were connected in series so that the DC voltage source amounted to 192 [V]. The inductors (10 mH/3.5 Apeak, Pony Electric Co., Gunma, Japan) were used as series reactors (L1, L2). The AC line filters (NAH-20-472-B, COSEL) were inserted at the output end of the reactors for noise reduction on the outputs. MWPE-IS-03 (Myway Plus Corp.) was used as the current sensor. A self-made sensor circuit was used for the voltage sensor considering the influence of noise. The developed control system was coded in C language, which was implemented on a DSP board (PE-Expert4, Myway Plus Corp.). The measurements through the current and voltage sensors were sent to PE-Expert4 as analog signals. Based on the measurements, the proposed control system generates gate signals using PWM to control the outputs of the inverter (MWINV-1R022, Myway Plus Corp.). The operating frequency of the PE-Expert4 is 1.25 GHz, and the carrier frequency of the PWM is 20 kHz. The experimental data were measured at a sampling frequency of 20 kHz using PE-View X. The voltage and current waveforms were observed through an oscilloscope. In this experiment, an AC power supply (EC1000SA, NF Corp.) was used as the grid-simulated power source. A lamp load (variable capacity up to 240 W) was connected in parallel to the inverters.

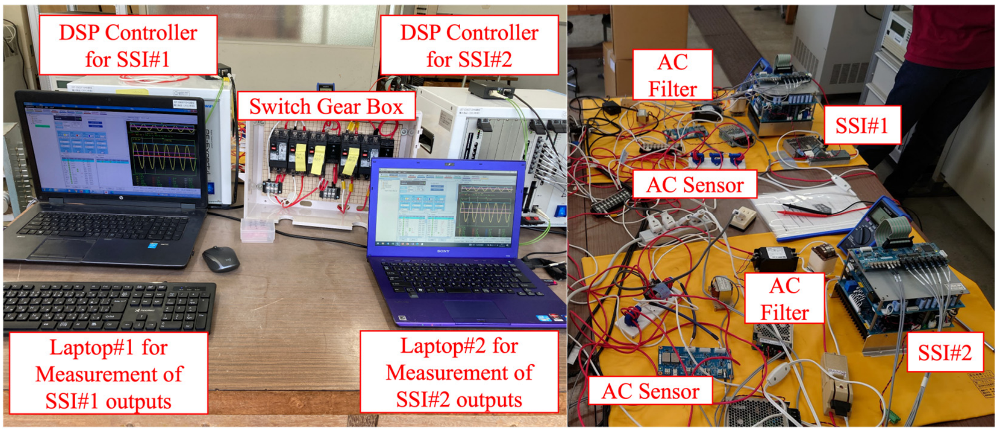

Figure 27. Constructed experimental devices.

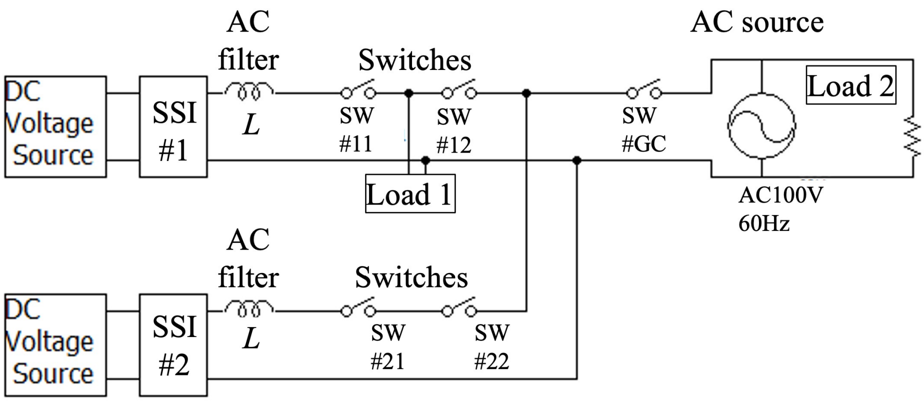

Figure 28. Electrical circuits for the SMG experiments.

Table 9. Parameters in the experimental circuit in Figure 28 (Reference [41]).

Parameters	Values
AC filter *L*	10 mH
Load 1	Light (AC100 V, 100 W) for the resistive load connection test
	Light (AC100 V, 20 W) for the lag load connection test and distortion load connection test
Load 2	Transformer (T-200, 2.1 kVA, Yamabishi, Tokyo, Japan) for the lag load connection test
	Switching regulator (PR18-3A, KENWOOD, Tokyo, Japan) for the lag load connection test
	Variable resistance (D-8, Yamabishi) for the lag load connection test

5.3.1. SMG Operation Test Connected to a Grid-Simulated Power Supply

An SMG operation test was performed in which two SSI units were operated synchronously, connected to the grid-simulated power supply. In this operation, two SSI units were supplied power from the power supply. Measurements in this operation obtained from PE-View X are shown in Figure 29. The yellow, red, and blue lines represent the voltage, current, and active power, respectively. We can observe stable SMG operation with two SSI units and the power source, where stable power charging from the grid-simulated power source to the individual batteries (DC voltage sources) through the SSI units.

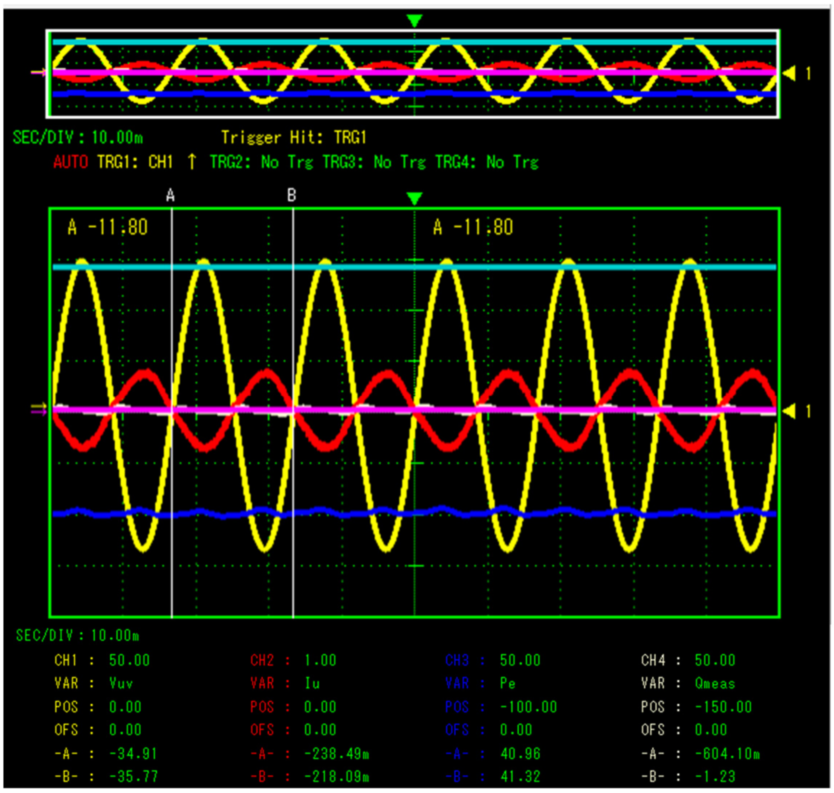

Figure 29. Result of grid-connected operation test (yellow: voltage waveform, sky blue: maximum value of voltage, dark blue: RMS value of voltage (minus value), red: current waveform, pink: reactive power).

5.3.2. Off-Grid SMG Operation Test under Various Load Conditions

We performed a series of off-grid SMG operation tests, disconnecting the grid-simulated power supply in Figure 28. The stability of the off-grid SMG operation with two SSI units is examined using three kinds of loads, which are a 100 W lamp load, inductive load, and a full-wave rectifier load including a ripple filter.

In the first experiment, a 100 W lamp load (LOAD1) was connected near SW#11. Figure 30 shows the waveforms of voltage and current in this operation. We see that SSI#1 and SSI#2 successfully provide power to the load with low distortion in terms of current waveforms. The current and voltage waveforms are in phase, implying that no reactive power was supplied. Total harmonic distortion (THD) was measured with a power quality analyzer, the results of which are shown in Figure 30. The results show that stable operation was performed without waveform distortions and voltage fluctuations.

Next, the connection was changed from the purely lamp load to the lagging load while maintaining off-grid operation. The load consisted of two 20 W lamp loads and four unloaded transformers of 1 kVA in parallel, representing an induction motor load with a power factor of approximately 0.8 lagging.

Figure 31 shows the results. There were almost no distortions in the voltage waveforms (THD = 1.44%). In the current waveforms, distortions were observed (THD = 16%). The current distortion is thought to be caused by iron core hysteresis in the transformer. This is a quite severe situation where the excitation current of the unloaded transformer is directly supplied as the lagging component. Nevertheless, both units successfully kept the stability of the off-grid SMG operation under such a severe lagging load.

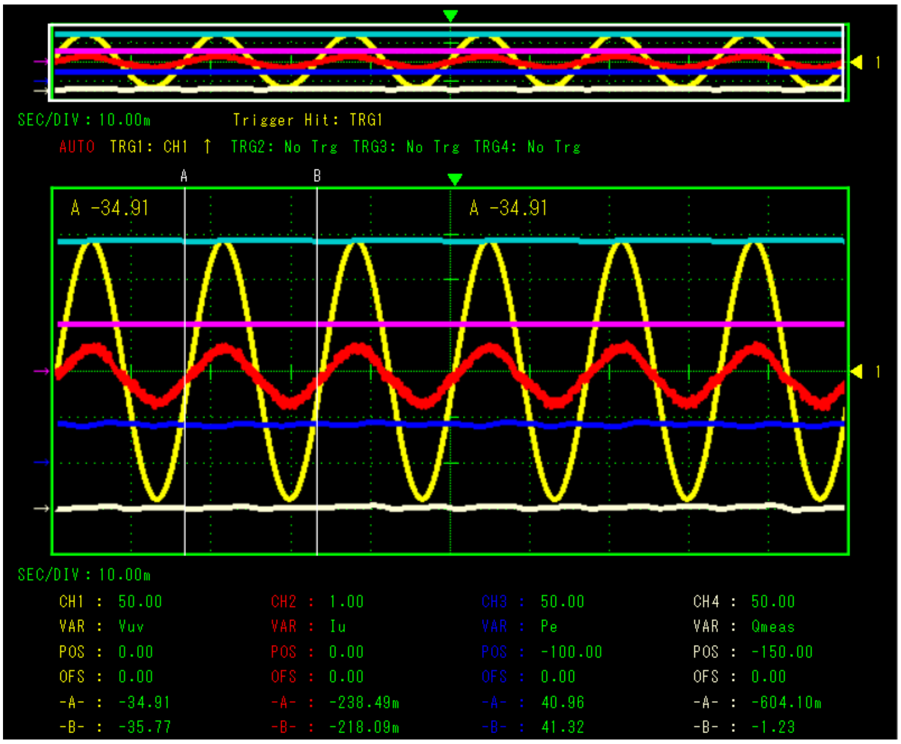

(**a**) V = 98.2 V THD = 0.35%
I_1 = 0.49 A THD = 1.53%

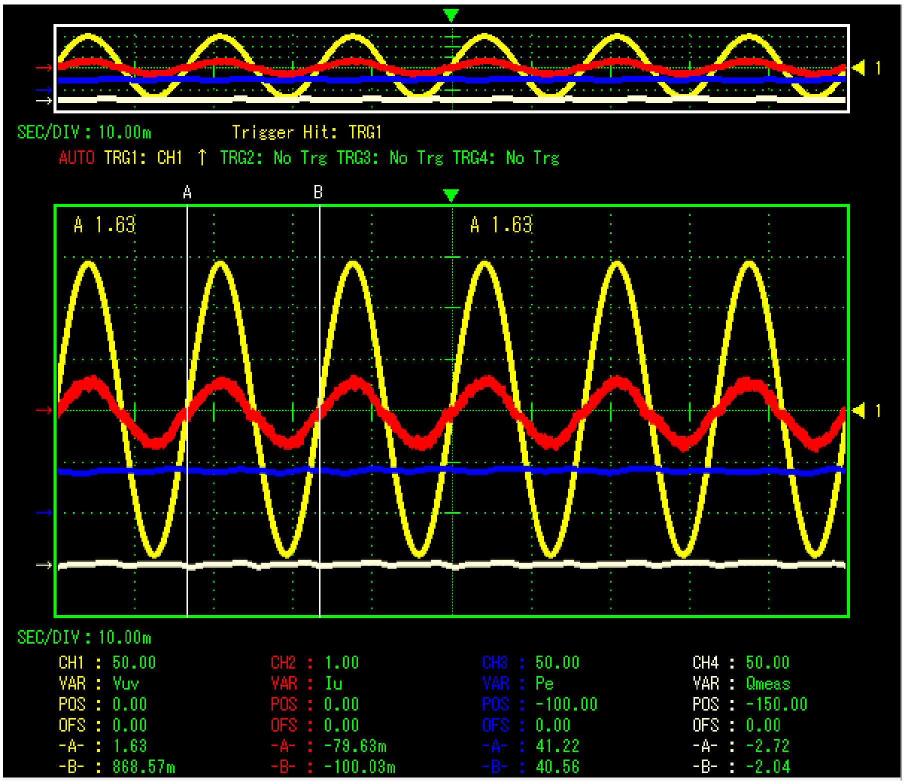

(**b**) I_2 = 0.49 A THD = 0.00%

Figure 30. Results of the off-grid operation test with a 100 W lamp load: (**a**) SSI #1; (**b**) SSI #2 (yellow: voltage waveform, red: current waveform, blue: active power, white: reactive power).

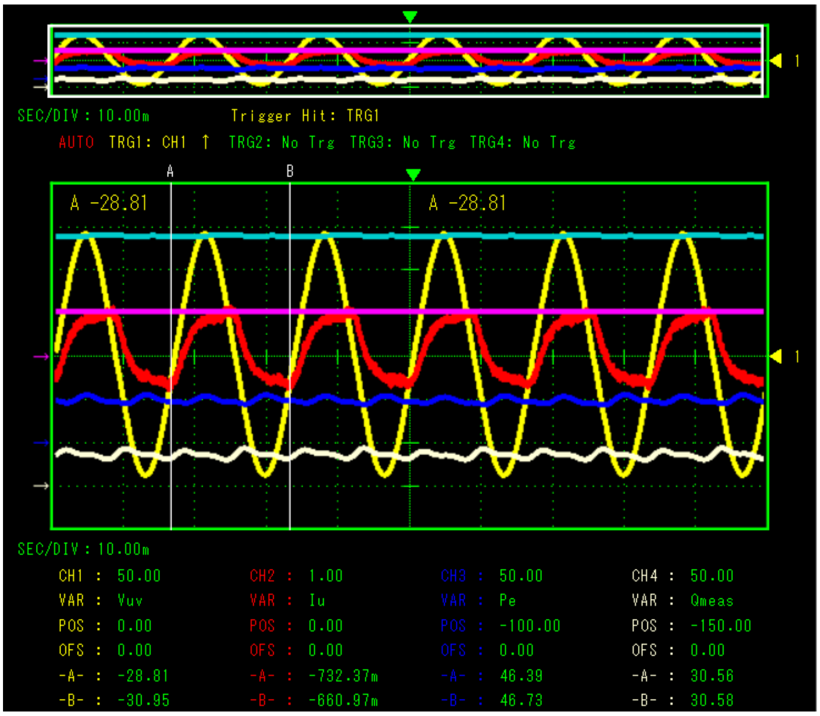

(**a**) V = 97.2 V THD = 1.44%, I_1 = 0.59 A P.F. = 0.796 THD = 16.66%

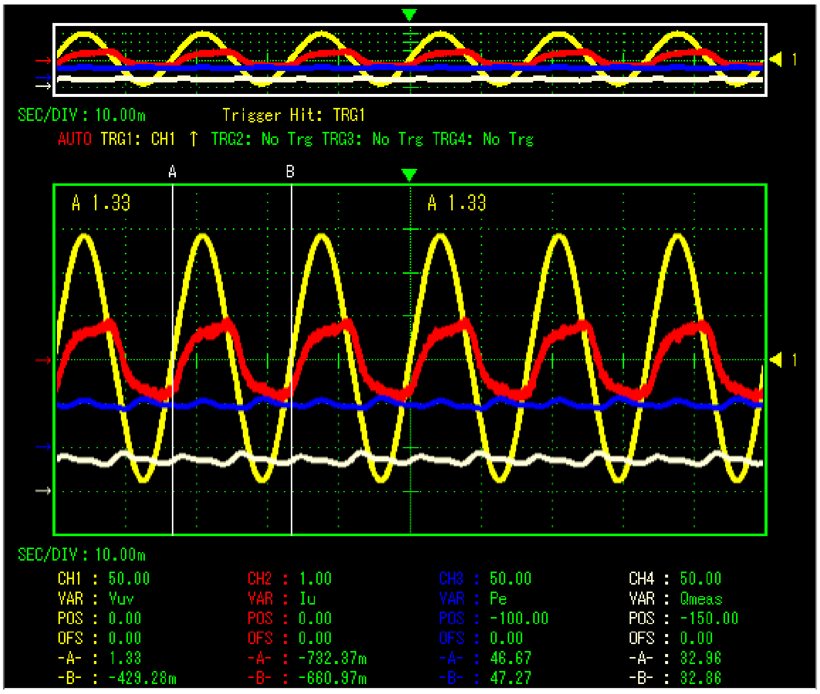

(**b**) I_2 = 0.59 A P.F. = 0.796 THD = 16.45%

Figure 31. Results of the off-grid operation test with the inductive load: (**a**) SSI #1; (**b**) SSI #2 (yellow: voltage waveform, red: current waveform, blue: active power, white: reactive power).

Finally, a 100 W lamp and a DC-power-supply were connected in parallel as AC loads in off-grid SMG operation. The latter load can generate a typical distortion current in a household appliance since it is equivalent to a full-wave rectifier circuit with a ripple filter. Thus, this case represents an extreme condition in possible operations with rectifier-based devices.

The results of the experiment are shown in Figure 32, where stable operation is confirmed. A typical distortion of the full-wave rectifier circuit is observed in the current waveform. Even with a large current distortion with a THD of 28% or more, it is confirmed that stable and reliable SMG operation was performed with slight distortion of the voltage waveform (THD = 3.42%).

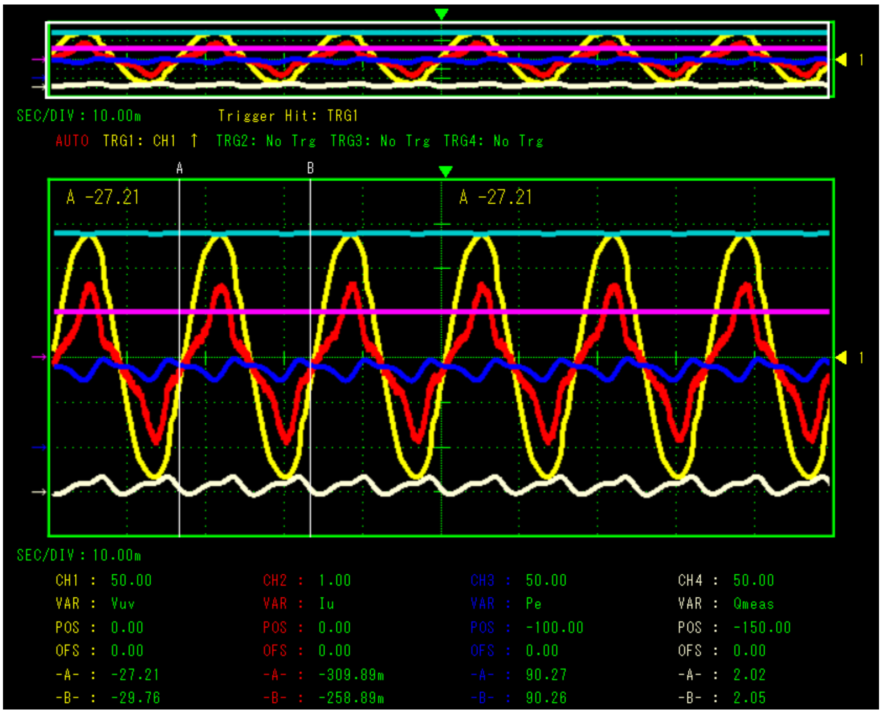

(**a**) V = 97.7 V THD = 3.42%, I_1 = 0.88 A THD = 29.82%

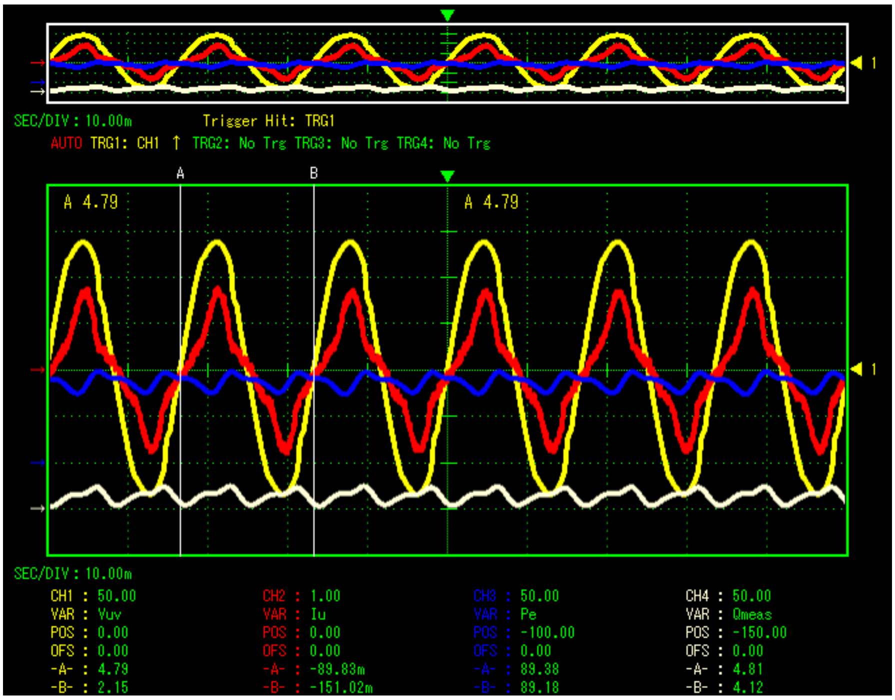

(**b**) I_2 = 0.88 A THD = 27.43%

Figure 32. Results of the off-grid operation test with extreme loads with rectifier-based devices: (**a**) SSI #1; (**b**) SSI #2 (yellow: voltage waveform, red: current waveform, blue: active power, white: reactive power).

The results of various loading tests show that the distortion factor of THD decreases under conditions of poor loading characteristics, as shown in Table 10. However, stable operation of the SSIs can be maintained, confirming that the performance is sufficient for the construction of an SMG.

Table 10. Results of the load connection tests.

(1) Grid-connection Test	No-load, depending on system voltage
(2) Resistive Load Connection Test	System Voltage: V = 98.2 V, THD = 0.35% SSI#1: I_1 = 0.49A, THD_1 = 1.53% SSI#2: I_2 = 0.49A, THD_2 = 0.00%
(3) Lag Load Connection Test	System Voltage: V = 97.2 V, THD = 1.44% SSI#1: I_1 = 0.59A, THD_1 = 16.66%, P.F. = 0.796 SSI#2: I_2 = 0.59A, THD_2 = 16.45%
(4) Distortion LoadConnection Test	System Voltage: V = 97.7 V, THD = 3.42% SSI#1: I_1 = 0.88A, THD_1 = 29.82% SSI#2: I_2 = 0.88A, THD_2 = 27.43%

The series of experimental studies in this section show that the proposed SMG provides reliable performance in both grid-connected and off-grid operations in cases with poor quality loads. The robust stability of the SMG consisting of two SSIs is confirmed as a basic characteristic even in conditions in which considerable current distortions are in existence under various load conditions.

6. Conclusions

This paper presents our recent progress on the SSI concerned with power system stabilization and SMG operations. Newly obtained contributions are as follows:

- An RMS simulation model was developed based on the NIC design method for stability analysis of a power system with SSIs as well as an SMG. The developed RMS model was accurate enough when compared with the experimental results. The error rate was about 10% for the maximum power swing (See Figure 10e, for example).
- Using the developed RMS analysis tool, the stabilization effects of the SSIs were investigated in the standard three-machine system. In the case where all PV inverters were replaced by SSIs on the demand side, considerable improvements were observed in terms of transient stability, small-signal stability, and frequency stability, where the frequency nadir was improved from −0.258 to −0.160, for example. (See Cases 2 and 4 in Table 7.)
- The performance of the SMG was demonstrated through experiments which show the feasibility and robust stability in terms of off-grid operations under various situations including ill-conditioned loads. (See the stable operation in Figure 32 for full-wave rectifier load.)

The above results imply that the proposed strategy of SMG is promising from the point of view of grid stability in a normal state as well as in off-grid operation of the SMG in an emergency state.

Future works are assumed as follows. Since the SMG allows flexible configurations (see Figure 22 for the power outage), further investigations are required for the stabilities of various patterns of the off-grid operations of individual SMGs. The construction of a three-phase MG using SMGs will also be part of a future study.

An important point in the construction of SMGs is that no major elements other than SSIs are necessary. SSIs are installed on the demand side by replacing conventional inverters for PVs, batteries, etc. Furthermore, no special operation costs are necessary in terms of grid operation since the SSIs work as demand-side devices, where basically no controls are required from the network operator. This implies that no major costs are necessary in a normal state of operation. This is a big difference compared with usual MG schemes which require a large cost expenditures for system controls.

Author Contributions: Conceptualization, S.S.; Methodology, N.Y., Y.Z., Y.S., S.S. and M.Y.; Software, Y.S. and S.S.; Validation, N.Y., Y.Z., S.S., F.K., T.F. and H.I.; Investigation, N.Y., Y.Z., Y.S., S.S., M.Y. and T.H.; Writing—original draft, N.Y., M.Y. and T.H.; Writing—review & editing, N.Y., Y.Z., Y.S. and S.S.; Supervision, N.Y.; Project administration, N.Y., Y.Z., F.K. and T.F. All authors have read and agreed to the published version of the manuscript.

Funding: This paper was supported by JSPS Grant-in-Aid for Scientific Research (KAKENHI JP20H00251), and Project, JPNP22003, commissioned by the New Energy and Industrial Technology Development Organization (NEDO).

Data Availability Statement: The data are not publicly available but can be provided on request.

Conflicts of Interest: The authors declare no conflicts of interest.

Abbreviations

The following abbreviations are used in this manuscript:

AC	Alternating Current
A/D	Analog-to-Digital Converter
AQR	Automatic Reactive Power Regulator
AVR	Automatic Voltage Regulator
CRIEPI	Central Research Institute of Electric Power Industry
DC	Direct Current
DSP	Digital Signal Processor
EMF	Electromotive Force
EMS	Energy Management System
FFR	Fast Frequency Response
GFL	Grid-Following
GFM	Grid-Forming
HIL	Hardware-In-the-Loop
HV	High-Voltage
IBR	Inverter-Based Resource
LV	Low-Voltage
MG	Microgrid
NEDO	New Energy and Industrial Technology Development Organization, National Research and Development Agency
NIC	Non-Interference Core
PI	Proportional Integration
PV	Photovoltaic Power Generation
Q-PI	Reactive Power Control with PI
RMS	Root Mean Square
RoCoF	Rate of Change of Frequency
SMG	Single-Phase Microgrid
SO-SOGI-QSG	Improved Second-Order–Second-Order Generalized Integrator based on Quadrature Signal Generation
SSI	Single-Phase Synchronous Inverter
THD	Total Harmonic Distortion
V-1L	Voltage Control with First-Order Delay
VRE	Variable Renewable Energy
VSCs	Voltage Source Converters
VSM	Virtual Synchronous Machine

Appendix A

Using the same test circuit as in Figure 6, additional experiments were conducted, where the same fault without fault clearance was applied. That is, the transient waveforms after a short-circuit fault at 0.4 s for 0° of fault timing with the different parameters are shown in Figure A1 with the same setting of ($\widetilde{M}$ and $\widetilde{D}$) and Figure A2 with these parameters increased. The other parameters were not changed. In both figures, (a) is the active power P_e [W] from the SSI and (b) is the system frequency f [Hz]. We can observe the typical transient behavior of the proposed SSI, similar to the conventional synchronous generators.

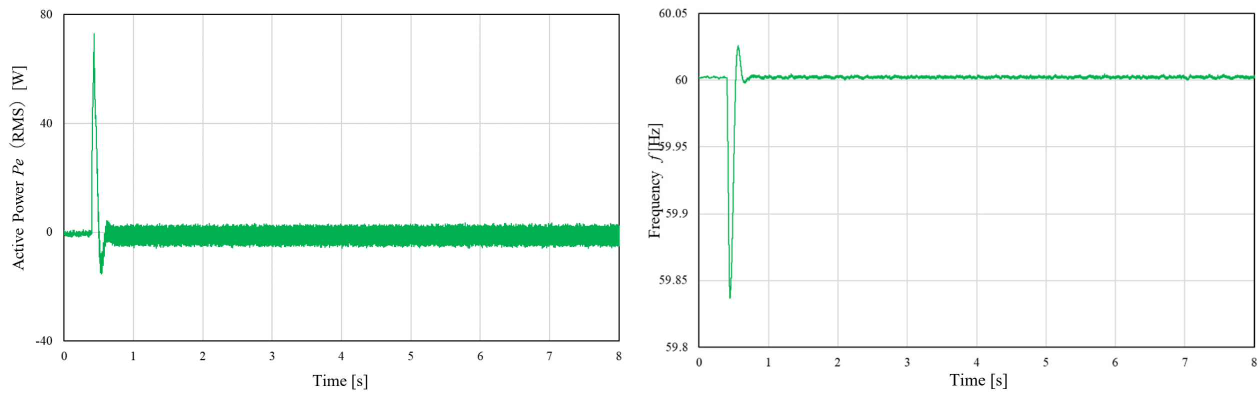

(**a**) (**b**)

Figure A1. Experimental results of the transient responses of a 0° fault timed at 0.4 s ($\widetilde{M}$ = 1, $\widetilde{D}$ = 50): (**a**) active power P_e [W]; (**b**) frequency f [Hz].

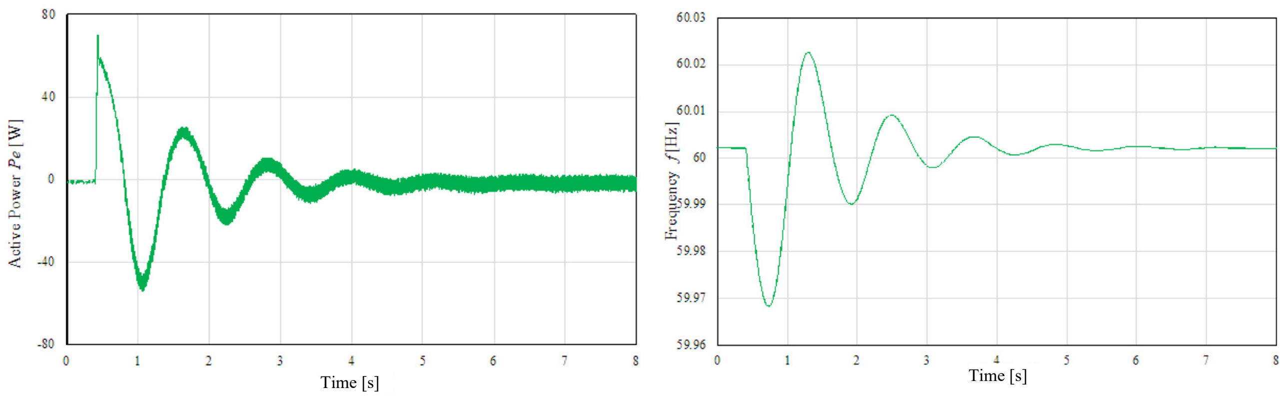

(**a**) (**b**)

Figure A2. Experimental results of the transient responses of a 0° fault timed at 0.4 s ($\widetilde{M}$ = 50, $\widetilde{D}$ = 100): (**a**) active power P_e [W]; (**b**) frequency f [Hz].

References

1. Tayyebi, A.; Groß, D.; Anta, A.; Kupzog, F.; Dörfler, F. Frequency Stability of Synchronous Machines and Grid-Forming Power Converters. *IEEE J. Emerg. Sel. Top. Power Electron.* **2020**, *8*, 1004–1018. [CrossRef]
2. Zhang, H.; Xiang, W.; Lin, W.; Wen, J. Grid Forming Converters in Renewable Energy Sources Dominated Power Grid: Control Strategy, Stability, Application, and Challenges. *J. Mod. Power Syst. Clean Energy* **2021**, *9*, 1239–1256. [CrossRef]
3. Wang, X.; Taul, M.G.; Wu, H.; Liao, Y.; Blaabjerg, F.; Harnefors, L. Grid-Synchronization Stability of Converter-Based Resources—An Overview. *IEEE Open J. Ind. Appl.* **2020**, *1*, 115–134. [CrossRef]
4. Laaksonen, H. Improvement of Power System Frequency Stability with Universal Grid-Forming Battery Energy Storages. *IEEE Access* **2023**, *11*, 10826–10841. [CrossRef]
5. Milano, F.; Dorfler, F.; Hug, G.; Hill, D.J.; Verbič, G. Foundations and challenges of low-inertia systems (Invited Paper). In Proceedings of the 2018 Power Systems Computation Conference (PSCC), Dublin, Ireland, 11–15 June 2018. [CrossRef]
6. Markovic, U.; Stanojev, O.; Aristidou, P.; Vrettos, E.; Callaway, D.; Hug, G. Understanding Small-Signal Stability of Low-Inertia Systems. *IEEE Trans. Power Syst.* **2021**, *36*, 3997–4017. [CrossRef]
7. Paolone, M.; Gaunt, T.; Guillaud, X.; Liserre, M.; Meliopoulos, S.; Monti, A.; Van Cutsem, T.; Vittal, V.; Vournas, C. Fundamentals of power systems modelling in the presence of converter-interfaced generation. *Electr. Power Syst. Res.* **2020**, *189*, 106811. [CrossRef]
8. Ahmed, F.; Kez, D.A.; McLoone, S.; Best, R.J.; Cameron, C.; Foley, A. Dynamic grid stability in low carbon power systems with minimum inertia. *Renew. Energy* **2023**, *210*, 486–506. [CrossRef]

9. Kez, D.A.; Foley, A.; Ahmed, F.; Morrow, D.J. Overview of frequency control techniques in power systems with high inverter-based resources: Challenges and mitigation measures. *IET Smart Grid* **2023**, *6*, 447–469. [CrossRef]
10. Li, L.; Zhu, D.; Zou, X.; Hu, J.; Kang, Y.; Guerrero, J.M. Review of frequency regulation requirements for wind power plants in international grid codes. *Renew. Sustain. Energy Rev.* **2023**, *187*, 113731. [CrossRef]
11. Hong, Q.; Khan, M.A.U.; Henderson, C.; Egea-Àlvarez, A.; Tzelepis, D.; Booth, C. Addressing Frequency Control Challenges in Future Low-Inertia Power Systems: A Great Britain Perspective. *Engineering* **2021**, *7*, 1057–1063. [CrossRef]
12. Su, L.; Qin, X.; Zhang, S.; Zhang, Y.; Jiang, Y.; Han, Y. Fast frequency response of inverter-based resources and its impact on system frequency characteristics. *Glob. Energy Interconnect.* **2020**, *3*, 475–485. [CrossRef]
13. D'Arco, S.; Suul, J.A.; Fosso, O.B. A Virtual Synchronous Machine implementation for distributed control of power converters in SmartGrids. *Electr. Power Syst. Res.* **2015**, *122*, 180–197. [CrossRef]
14. D'Arco, S.; Suul, J.A. Equivalence of virtual synchronous machines and frequency-droops for converter-based Microgrids. *IEEE Trans. Smart Grid* **2014**, *5*, 394–395. [CrossRef]
15. Gunasekara, R.; Muthumuni, D.; Filizadeh, S.; Kho, D.; Marshall, B.; Ponnalagan, B.; Adeuyi, O.D. A Novel Virtual Synchronous Machine Implementation and Verification of Its Effectiveness to Mitigate Renewable Generation Connection Issues at Weak Transmission Grid Locations. *IET Renew. Power Gener.* **2022**, *17*, 2433–2678. [CrossRef]
16. Zhong, Q.C.; Weiss, G. Synchronverters: Inverters that mimic synchronous generators. *IEEE Trans. Ind. Electron.* **2011**, *58*, 1259–1267. [CrossRef]
17. Kryonidis, G.C.; Malamaki, K.N.D.; Mauricio, J.M.; Demoulias, C.S. A New Perspective on the Synchronverter Model. *Int. J. Electr. Power Energy Syst.* **2022**, *140*, 108072. [CrossRef]
18. Zhang, L.; Harnefors, L.; Nee, H.P. Power-synchronization control of grid-connected voltage-source converters. *IEEE Trans. Power Syst.* **2010**, *25*, 809–820. [CrossRef]
19. Alawasa, K.M.; Mohamed, Y.A.R.I. Impedance and damping characteristics of grid-connected VSCs with power synchronization control strategy. *IEEE Trans. Power Syst.* **2015**, *30*, 952–961. [CrossRef]
20. Tayab, U.B.; Roslan, M.A.B.; Hwai, L.J.; Kashif, M. A review of droop control techniques for microgrid. *Renew. Sustain. Energy Rev.* **2017**, *76*, 717–727. [CrossRef]
21. Sekizaki, S.; Nakamura, Y.; Sasaki, Y.; Yorino, N.; Zoka, Y.; Nishizaki, I. A development of pseudo-synchronizing power VSCs controller for grid stabilization. In Proceedings of the 2016 Power Systems Computation Conference (PSCC), Genoa, Italy, 20–24 June 2016. [CrossRef]
22. Sekizaki, S.; Yorino, N.; Sasaki, Y.; Matsuo, K.; Nakamura, Y.; Zoka, Y.; Shimizu, T.; Nishizaki, I. Proposal of a single-phase synchronous inverter with noninterference performance for power system stability enhancement and emergent microgrid operation. *Electr. Eng. Jpn.* **2019**, *207*, 3–13, Original paper: *IEEJ Trans. Power Energy* **2018**, *138*, 893–901. [CrossRef]
23. EU Project POSYTYF—Powering System Flexibility in the Future Renewable Energy Sources, On-Going as of 2023. Available online: https://posytyf-h2020.eu/ (accessed on 8 January 2024).
24. US Project Unifi (Universal Interoperability for Grid-Forming Inverters)—Unifing Inverters and Grids, On-Going as of 2023. Available online: https://sites.google.com/view/unifi-consortium/home (accessed on 8 January 2024).
25. Australia ARENA Project Broken Hill Battery Energy Storage System, On-Going as of 2023. Available online: https://arena.gov.au/projects/agl-broken-hill-grid-forming-battery/ (accessed on 8 January 2024).
26. Marinescu, S.; Gomis-Bellmunt, O.; Dörfler, F.; Schulte, H.; Sigrist, L. Dynamic Virtual Power Plant: A New Concept for Grid Integration of Renewable Energy Sources. *IEEE Access* **2022**, *10*, 104980–104995. [CrossRef]
27. Collados-Rodriguez, C.; Spier, W.D.; Cheah-Mane, M.; Prieto-Araujo, E.; Gomis-Bellmunt, O. Preventing loss of synchronism of droop-based grid-forming converters during frequency excursions. *Int. J. Electr. Power Energy Syst.* **2023**, *148*, 108989. [CrossRef]
28. Collados-Rodríguez, C.; Antolí-Gil, E.; Sánchez-Sánchez, E.; Girona-Badia, J.; Lacerda, V.A.; Cheah-Mañe, M.; Prieto-Araujo, E.; Gomis-Bellmunt, O. Definition of Scenarios for Modern Power Systems with a High Renewable Energy Share. *Glob. Chall.* **2023**, *7*, 2200129. [CrossRef] [PubMed]
29. Lacerda, V.A.; Araujo, E.P.; Chea-Mañe, M.; Gomis-Bellmunt, O. Phasor and EMT models of grid-following and grid-forming converters for short-circuit simulations. *Electr. Power Syst. Res.* **2023**, *223*, 109662. [CrossRef]
30. Liu, Y.; Huang, R.; Du, W.; Singhal, A.; Huang, Z. Highly-Scalable Transmission and Distribution Dynamic Co-Simulation with 10,000+ Grid-Following and Grid-Forming Inverters. *IEEE Trans. Power Deliv.* 2023, 1–12, *Early Access*. [CrossRef]
31. Lu, M.; Cai, W.; Dhople, S.; Johnson, B. Large-signal Stability of Phase-balanced Equilibria in Single-phase Grid-forming Inverter Systems. *IEEE Trans. Power Electron.* **2023**, 1–14, *Early Access*. [CrossRef]
32. Islam, M.D.; Muttaqi, K.M.; Sutanto, D.; Rahman, M.M.; Alonso, O. Design of a Controller for Grid Forming Inverter-Based Power Generation Systems. *IEEE Access* **2023**, *11*, 2169–3536. [CrossRef]
33. Areed, E.F.; Yan, R.; Saha, T.K. Impact of Battery Ramp Rate Limit on Virtual Synchronous Machine Stability During Frequency Events. *IEEE Trans. Sustain. Energy* **2024**, *15*, 567–580. [CrossRef]
34. Yorino, N.; Sekizaki, S.; Adachi, K.; Sasaki, Y.; Zoka, Y.; Bedawy, A.; Shimizu, T.; Amimoto, K. A Novel Design of Single-phase Microgrid Based on Non-Interference Core Synchronous Inverters for Power System Stabilization. *IET Gener. Transm. Distrib.* **2022**, *17*, 2861–2875. [CrossRef]

35. Farrokhabadi, M.; Canizares, C.A.; Simpson-Porco, J.W.; Nasr, E.; Fan, L.; Mendoza-Araya, P.A.; Tonkoski, R.; Tamrakar, U.; Hatziargyriou, N.; Lagos, D.; et al. Microgrid Stability Definitions, Analysis, and Examples. *IEEE Trans. Power Syst.* **2020**, *35*, 3513–3529. [CrossRef]
36. Sekizaki, S.; Matsuo, K.; Sasaki, Y.; Yorino, N.; Nakamura, Y.; Zoka, Y.; Shimizu, T.; Nishizaki, I. A Development of Single-phase Synchronous Inverter and Integration to Single-phase Microgrid effective for frequency stability enhancement. *IFAC-Pap. OnLine* **2018**, *51*, 245–250. [CrossRef]
37. Yorino, N.; Sasaki, H.; Masuda, Y.; Tamura, Y.; Kitagawa, M.; Oshimo, A. An investigation of voltage instability problems. *IEEE Trans. Power Syst.* **1992**, *7*, 600–611. [CrossRef]
38. Sekizaki, S.; Yorino, N.; Sasaki, Y.; Zoka, Y.; Shimizu, T.; Nishizaki, I. Single-phase Synchronous Inverter with Overcurrent Protection using Current Controller with Latched Limit Strategy. *IEE J. Trans. Electr. Electron. Eng.* **2021**, *18*, 1001–1014. [CrossRef]
39. Xin, Z.; Wang, X.; Qin, Z.; Lu, M.; Loh, P.C.; Blaabjerg, F. An Improved Second-Order Generalized Integrator Based Quadrature Signal Generator. *IEEE Trans. Power Electron.* **2016**, *31*, 8068–8073. [CrossRef]
40. Anderson, P.M.; Fouad, A.A. *Power System Control and Stability*, 2nd ed.; Wiley—IEEE Press: Hoboken, NJ, USA, 2003.
41. KAKEN—Research Projects | Construction of a Single-Phase Microgrid Using an Actual Machine (KAKENHI-PROJECT-20H00251). Available online: https://kaken.nii.ac.jp/en/grant/KAKENHI-PROJECT-20H00251/ (accessed on 22 October 2021).